Journal of Computational and Applied Mathematics 235 (2011) 5056–5077

Contents lists available at ScienceDirect

Journal of Computational and Applied Mathematics

journal homepage: www.elsevier.com/locate/cam

Implicit finite element schemes for stationary compressible particle-laden gas flows

Marcel Gurris [a,*], Dmitri Kuzmin [b], Stefan Turek [a]

[a] Dortmund University of Technology, Institute of Applied Mathematics, Vogelpothsweg 87, D-44227 Dortmund, Germany

[b] University of Erlangen-Nürnberg, Chair of Applied Mathematics III, Haberstr. 2, D-91058 Erlangen, Germany

ARTICLE INFO

Article history:
Received 1 September 2010
Received in revised form 22 April 2011

Keywords:
Particle-laden gas flows
Two-fluid model
High-resolution schemes
Boundary conditions
Implicit schemes
Stationary flow

ABSTRACT

The derivation of macroscopic models for particle-laden gas flows is reviewed. Semi-implicit and Newton-like finite element methods are developed for the stationary two-fluid model governing compressible particle-laden gas flows. The Galerkin discretization of the inviscid fluxes is potentially oscillatory and unstable. To suppress numerical oscillations, the spatial discretization is performed by a high-resolution finite element scheme based on algebraic flux correction. A multidimensional limiter of TVD type is employed. An important goal is the efficient computation of stationary solutions in a wide range of Mach numbers. This is a challenging task due to oscillatory correction factors associated with TVD-type flux limiters and the additional strong nonlinearity caused by interfacial coupling terms. A semi-implicit scheme is derived by a time-lagged linearization of the nonlinear residual, and a Newton-like method is obtained in the limit of infinite CFL numbers. The original Jacobian is replaced by a low-order approximation. Special emphasis is laid on the numerical treatment of weakly imposed boundary conditions. It is shown that the proposed approach offers unconditional stability and faster convergence rates for increasing CFL numbers. The strongly coupled solver is compared to operator splitting techniques, which are shown to be less robust.

1. Introduction

Significant advances have been achieved in the numerical modeling of flow phenomena. The governing models became more and more complex in recent years. Due to improved computing resources even the simulation of coupled flow phenomena like gas–particle suspensions is possible.

The so-called two-fluid model represents a system of macroscopic conservation laws for each phase. Typical standard discretizations, including those based on finite element methods, tend to produce numerical oscillations if they are applied to hyperbolic equations (or systems). This is unacceptable if the two-fluid model governing particle-laden gas flows is considered. From the physical point of view quantities like pressure and density have to be positive. This property can however be violated by the presence of undershoots and overshoots. To prevent the birth and growth of wiggles and preserve the physical properties of the solution, a suitable stabilization term should be added to the discretized equations. Kuzmin et al. [1–7] have developed a new approach to the design of high-resolution finite element schemes. Within the framework of algebraic flux correction, the coefficients of a standard Galerkin discretization are constrained using flux limiters based on a generalization of flux-corrected transport (FCT) algorithms and total variation diminishing (TVD) methods. As demonstrated in [8], algebraic flux correction is more reliable than mainstream stabilization/shock capturing techniques. The linearized

* Corresponding author. Fax: +49 231 5933.
E-mail addresses: marcel.gurris@math.uni-dortmund.de, marci0807@web.de (M. Gurris).

0377-0427/$ – see front matter © 2011 Elsevier B.V. All rights reserved.
doi:10.1016/j.cam.2011.04.036

FCT algorithm [5,7] is to be recommended for transient flows, whereas flux limiters of TVD type are better suited for the computation of steady-state solutions which is of primary interest in the present numerical study. Hence, the latter limiting strategy is adopted.

Implicit schemes will be possibly unconditionally stable if they are designed in a proper way. Since the convergence to steady-state depends on the propagation speed of the error waves, large CFL numbers accelerate the convergence to steady state. The implicit Euler approach corresponds to upwinding in time and therefore enjoys very useful numerical properties. This makes the backward Euler scheme a favorable choice in steady-state computations and it is therefore applied in this study. On the other hand, nonlinear systems must be solved and the computation of the nonlinear preconditioner is a challenging task. To avoid computationally expensive nonlinear iterations, we linearize fluxes and source terms around the current time level using a Taylor series expansion. This results in a coupled semi-implicit scheme. In our scheme we replace the original flux Jacobian by a low-order approximation, which reduces the computational costs and memory requirements and yields a robust solver. The source term Jacobian can be derived analytically [9], where the non-smooth parts are treated as constants. The computation of stationary solutions to hyperbolic equations is rarely performed with implicit solvers. Their development has been pursued by several groups [10–13] for the Euler equations. However, many existing schemes employ linearizable/differentiable limiters, are conditionally stable, and the rate of steady-state convergence deteriorates if the CFL number exceeds a certain upper bound. The scheme presented here converges for arbitrary CFL numbers despite oscillatory correction factors and the rate of steady-state convergence does not deteriorate for large CFL numbers. In the limit of infinite CFL numbers our scheme becomes a Newton-like method.

Boundary conditions are an important part of the discretization and the iterative solver. An inaccurate treatment of boundary conditions results in a loss of accuracy and may aggravate stability restrictions. It was already shown that weakly imposed boundary conditions provide superior robustness and convergence compared to their strongly imposed counterparts, while they maintain accuracy. Therefore, boundary conditions are imposed weakly in this research article.

The design of numerical solvers for the two-fluid model is a very challenging task since additional nonlinearities arise due to large and stiff algebraic coupling terms, which must be integrated and discretized in a proper way. Algebraic source terms are typically incorporated into the computational model making use of operator splitting [14–17]. We compare both, the strongly coupled method, where the fluxes and source terms are treated semi-implicitly, and the operator splitting approach in a numerical study. Furthermore, we show that operator splitting is inappropriate for steady-state simulations and subject to restrictive time step constraints. It may even inhibit convergence to a steady-state solution. The algorithm developed in this paper features most properties of the single-phase gas solver proposed in [9,18].

In the following sections we describe the design of high-resolution schemes for the two-fluid model, report the treatment of boundary conditions, and introduce the semi-implicit solver. Operator splitting techniques as well as a fully coupled approach are presented and compared in a numerical study.

2. Modeling

It is generally accepted that single-phase gas flows can be modeled by macroscopic equations of mass, momentum and energy conservation. The particulate (or dispersed) phase is also supposed to admit a continuous description. As a natural assumption, the single-phase equations are also valid for multi-phase flows except at the interfaces separating the different components. A mixture of two or more different materials can be interpreted as a flow, which is subdivided into single-phase regions by infinitesimal thin interfaces. Due to limited computing resources it is impossible to locate the interfaces at the microscopic scale if the dispersed phase is distributed over the whole domain. It is necessary to transform the microscopic equations into their macroscopic counterparts. In this case, macroscopic equations are derived by using suitable averaging procedures so that they are related to the microscopic ones in a mathematical sense.

Various techniques are reported in the literature and typical candidates are volume, time, statistical, and ensemble averages, which yield comparable results. A survey can be found in the textbooks of Drew and Passmann [19] and Ishii and Hibiki [20], where the latter text mainly focuses on time averaging. The different techniques typically yield similar results. The averaged equations are widely accepted and applied in a large number of publications. Saurel and Abgrall [17] derive a quite general hyperbolic non-conservative model, which is applicable to dense and dilute flows alike. Städke [21] used averaged hyperbolic equations for the numerical simulation of the interaction of water and steam. Such macroscopic two-fluid models were successfully applied to incompressible bubbly flows [22,23]. Computational models related to particle-laden gas flows can be found in [16,24,25,15,26,14,27–30]. The models employed for the different flow regimes widely agree in modeling aspects, except in the treatment of interface exchange. Although the interaction between the involved materials at the interfaces has a strong influence on the flow behavior and the simulation results, the modeling of some terms (e.g. lift forces) remains controversial in the literature. Consequently, the interface exchange should be modeled carefully.

Modeling of compressible particle-laden gas flows requires several assumptions and simplifications. This study is based on the following assumptions:

- No chemical reactions and no change of aggregate states.
- Both particles and gas are distributed over the whole domain.
- The inviscid equations of mass, momentum, and energy conservation are valid in the interior of each phase.
- The gas pressure satisfies the ideal gas law.

- There is no considerable amount of particle collisions and the particles do not interact with each other.
- The material density of the particles is constant. That means, the particulate phase is incompressible.
- Dilute flow conditions, i.e. the volume occupied by the particles is small.
- The material density ratio $\frac{\rho_g}{\rho_p} \ll 1$ is small.
- The particles are solid, spherical, of uniform size and their diameter is small compared to the length scale.
- The influences of curvature is negligible and surface tension does not play a role for solid particles.
- There are interfacial momentum and heat transfer, but no external momentum and energy sources.

In the following the index k refers to either the gas phase g or the particulate phase p. The interface quantities are denoted by the index int. Each phase satisfies a system of microscopic conservation laws that can be written as

$$\begin{aligned}
&\partial_t \rho_k + \nabla \cdot (\rho_k \mathbf{v}_k) = 0\\
&\partial_t (\rho_k \mathbf{v}_k) + \nabla \cdot (\rho_k \mathbf{v}_k \otimes \mathbf{v}_k + \mathbf{T}_k) = 0\\
&\partial_t (\rho_k E_k) + \nabla \cdot (\mathbf{v}_k \rho_k E_k + \mathbf{v}_k \cdot \mathbf{T}_k + \mathbf{q}_k) = 0,
\end{aligned} \tag{1}$$

where external body forces (like gravity) and heat sources are neglected. Density, velocity, and the heat flux of the individual phases are indicated by, ρ_k, $\mathbf{v}_k$, and $\mathbf{q}_k$, respectively. $\mathbf{T}_k$ denotes the stress tensor. Eq. (1) are valid for both phases exclusively in their interior Ω_k. To derive macroscopic equations which are valid in the whole domain we apply the volume averaging process [19]. The result is a coupled set of eight (in two dimensions) nonlinear conservation

$$\begin{aligned}
&\partial_t (\alpha_k \rho_k) + \nabla \cdot (\alpha_k \rho_k \mathbf{v}_k) = 0\\
&\partial_t (\alpha_k \rho_k \mathbf{v}_k) + \nabla \cdot (\alpha_k \rho_k \mathbf{v}_k \otimes \mathbf{v}_k + \alpha_k \mathbf{T}_k) = \mathbf{T}_k^{\text{int}} \cdot \nabla \alpha_k + \mathbf{F}_k^{\text{int}}\\
&\partial_t (\alpha_k \rho_k E_k) + \nabla \cdot (\alpha_k (\rho_k \mathbf{v}_k E_k + \mathbf{v}_k \cdot \mathbf{T}_k + \mathbf{q}_k)) = (\mathbf{v}_{\text{int}} \cdot \mathbf{T}_k^{\text{int}}) \cdot \nabla \alpha_k + \mathbf{v}_{\text{int}} \cdot \mathbf{F}_k^{\text{int}} + \alpha_k q_k^{\text{int}},
\end{aligned} \tag{2}$$

where α_k is the volume fraction. This system of macroscopic conservation laws is valid in the whole domain $\Omega = \Omega_g \cup \Omega_p$. The left hand side of this system contains convective terms for both phases, while the interface exchange terms are located on the right hand side. Both phases are coupled at the interface by the interfacial stress $\mathbf{T}_k^{\text{int}}$ and velocity $\mathbf{v}_{\text{int}}$, heat exchange q_k^{int}, interfacial forces $\mathbf{F}_k^{\text{int}}$, and the volume fractions. Eq. (2) are widely accepted as the general form of governing equations of two-phase flows. In our model external heat sources, viscosity, and body forces are neglected, while the interface terms $\mathbf{v}_{\text{int}}$, $\mathbf{T}_k^{\text{int}}$, q_k^{int}, and $\mathbf{F}_k^{\text{int}}$ require further modeling. Since the density ratio $\frac{\rho_g}{\rho_p} \ll 1$ is small, the impact of the interfacial forces except viscous drag is negligible [9]. Therefore, the only interfacial force, which is modeled in the present study, is viscous drag. For the inviscid equations the stress tensor is given in terms of

$$\mathbf{T}_k = \mathbf{I} P_k. \tag{3}$$

In the case of particle-laden gas flow under consideration the generic model (2) can be simplified to [9]

$$\begin{aligned}
&\partial_t (\alpha_g \rho_g) + \nabla \cdot (\alpha_g \rho_g \mathbf{v}_g) = 0\\
&\partial_t (\alpha_g \rho_g \mathbf{v}_g) + \nabla \cdot (\alpha_g \rho_g \mathbf{v}_g \otimes \mathbf{v}_g + \alpha_g \mathbf{I} P) = -\mathbf{F}_D\\
&\partial_t (\alpha_g \rho_g E_g) + \nabla \cdot \left(\alpha_g \mathbf{v}_g \left(\rho_g E_g + P\right)\right) = -\mathbf{v}_p \cdot \mathbf{F}_D - Q_T\\
&\partial_t (\alpha_p \rho_p) + \nabla \cdot (\alpha_p \rho_p \mathbf{v}_p) = 0\\
&\partial_t (\alpha_p \rho_p \mathbf{v}_p) + \nabla \cdot (\alpha_p \rho_p \mathbf{v}_p \otimes \mathbf{v}_p) = \mathbf{F}_D\\
&\partial_t (\alpha_p \rho_p E_p) + \nabla \cdot (\alpha_p \rho_p \mathbf{v}_p E_p) = \mathbf{v}_p \cdot \mathbf{F}_D + Q_T,
\end{aligned} \tag{4}$$

where

$$\mathbf{F}_D = \frac{3}{4} \alpha_p \frac{\rho_g}{d} C_D |\mathbf{v}_g - \mathbf{v}_p| (\mathbf{v}_g - \mathbf{v}_p) \tag{5}$$

is the drag force. The amount of drag depends on the drag coefficient C_D. This dimensionless quantity is defined by the (widely accepted) standard equation

$$C_D = \begin{cases} \dfrac{24}{\text{Re}} (1 + 0.15 \text{Re}^{0.687}) & \text{if Re} < 1000\\ 0.44 & \text{if Re} \geq 1000. \end{cases} \tag{6}$$

It is valid for spherical particles and given as a function of the particle Reynolds number Re [31]

$$\text{Re} = \frac{\rho_g d |\mathbf{v}_g - \mathbf{v}_p|}{\mu}. \tag{7}$$

Here μ denotes the microscopic dynamic viscosity of the gas and d is the particle diameter. Both μ and d are assumed to be constant. Sommerfeld [32] argues that the standard drag coefficient is a valid choice for steady flow problems. The rate of

interfacial heat transfer is given by [33]

$$Q_T = \frac{\mathrm{Nu}6\kappa}{d^2}\alpha_p(T_g - T_p) \tag{8}$$

as a function of the Nusselt number

$$\mathrm{Nu} = 2 + 0.65\mathrm{Re}^{\frac{1}{2}}\,\mathrm{Pr}^{\frac{1}{3}}, \qquad \mathrm{Pr} = \frac{c_{pg}\mu}{\kappa}. \tag{9}$$

The thermal conductivity κ, Prandtl number Pr, and heat capacity at constant pressure c_{pg} are assumed to be constant.

Moreover, the gas pressure is assumed to satisfy the ideal gas law

$$P = (\gamma - 1)\rho_g\left(E_g - \frac{|\mathbf{v}_g|^2}{2}\right) \tag{10}$$

and the pressure of the particulate phase is neglected [9] since particle collisions are insignificant under dilute flow conditions. Constitutive equations

$$T_k = \frac{1}{c_{vk}}\left(E_k - \frac{1}{2}|\mathbf{v}_k|^2\right) \tag{11}$$

link the temperature of both phases to the velocity and total energy. Note that the effective density $\alpha_p\rho_p$ is variable, although the particulate phase is incompressible with a constant material density ρ_p.

2.1. Mathematical properties

In this section we review important mathematical properties of governing equations (4). They can be written in a compact form

$$\partial_t U + \nabla\cdot\mathbf{F} = \tilde{S}, \tag{12}$$

where U is vector of conservative variables, $\mathbf{F}$ is the flux tensor, and $\tilde{S}$ are the source terms. Unfortunately, the governing equations lack hyperbolicity since there is no complete set of eigenvectors. Hence, the application of hyperbolic solvers, which are build on a diagonalization of the flux Jacobians is not directly possible. Neglecting the source terms we obtain a system of conservation laws for both phases. The equations governing the gas phase provide a complete set of eigenvectors and they coincide with the Euler equations for the effective density $\alpha_g\rho_g$. On the other hand the equations modeling the particulate phase are a coupled set of pressureless transport equations. We recommend to compute the stabilization and prescribe boundary conditions separately for both phases, while the nonlinear system should be solved in a strongly coupled way. Since the treatment of the gas phase is described in [9,2,18], we focus our attention to the pressureless conservation laws of the particulate phase.

To avoid confusion and simplify notation, the index p, denoting the particulate phase, will be dropped in the remainder of this section. Neglecting the right hand sides of Eqs. (4), the two-dimensional system of conservation laws that govern the motion of particles can be written as

$$\partial_t\begin{bmatrix}\rho\\ \rho\mathbf{v}\\ \rho E\end{bmatrix} + \nabla\cdot\begin{bmatrix}\rho\mathbf{v}\\ \rho\mathbf{v}\otimes\mathbf{v}\\ \rho E\mathbf{v}\end{bmatrix} = 0 \tag{13}$$

or simply

$$\partial_t U + \nabla\cdot\mathbf{F} = \partial_t U + \partial_x F^{(x)} + \partial_y F^{(y)} = 0. \tag{14}$$

In the former equation $U = (\rho, \rho u, \rho v, \rho E)^T = (U^{(1)}, U^{(2)}, U^{(3)}, U^{(4)})$ is the vector of conservative variables. The effective density is given by $\rho = \alpha_p\rho_p$, and $\mathbf{v} = (u, v)^T$ denotes the velocity vector. The inviscid flux vectors

$$F^{(x)} = \begin{bmatrix}\rho u\\ \rho u^2\\ \rho uv\\ \rho Eu\end{bmatrix} = \begin{bmatrix}U^{(2)}\\ \dfrac{U^{(2)^2}}{U^{(1)}}\\ \dfrac{U^{(2)}U^{(3)}}{U^{(1)}}\\ \dfrac{U^{(2)}U^{(4)}}{U^{(1)}}\end{bmatrix} \quad\text{and}\quad F^{(y)} = \begin{bmatrix}\rho v\\ \rho uv\\ \rho v^2\\ \rho Ev\end{bmatrix} = \begin{bmatrix}U^{(3)}\\ \dfrac{U^{(2)}U^{(3)}}{U^{(1)}}\\ \dfrac{U^{(3)^2}}{U^{(1)}}\\ \dfrac{U^{(3)}U^{(4)}}{U^{(1)}}\end{bmatrix} \tag{15}$$

define the rate of convective transport along the corresponding axes of the two-dimensional Cartesian reference frame. The tensor of all convective fluxes is denoted by

$$\mathbf{F} = (F^{(x)}, F^{(y)}). \tag{16}$$

The flux Jacobians for both directions are given by

$$\frac{\partial F^{(x)}}{\partial U} = \begin{bmatrix} 0 & 1 & 0 & 0 \\ -\dfrac{U^{(2)^2}}{U^{(1)^2}} & 2\dfrac{U^{(2)}}{U^{(1)}} & 0 & 0 \\ -\dfrac{U^{(2)}U^{(3)}}{U^{(1)^2}} & \dfrac{U^{(3)}}{U^{(1)}} & \dfrac{U^{(2)}}{U^{(1)}} & 0 \\ -\dfrac{U^{(2)}U^{(4)}}{U^{(1)^2}} & \dfrac{U^{(4)}}{U^{(1)}} & 0 & \dfrac{U^{(2)}}{U^{(1)}} \end{bmatrix} = \begin{bmatrix} 0 & 1 & 0 & 0 \\ -u^2 & 2u & 0 & 0 \\ -uv & v & u & 0 \\ -uE & E & 0 & u \end{bmatrix} \tag{17}$$

and

$$\frac{\partial F^{(y)}}{\partial U} = \begin{bmatrix} 0 & 0 & 1 & 0 \\ -\dfrac{U^{(2)}U^{(3)}}{U^{(1)^2}} & \dfrac{U^{(3)}}{U^{(1)}} & \dfrac{U^{(2)}}{U^{(1)}} & 0 \\ -\dfrac{U^{(3)^2}}{U^{(1)^2}} & 0 & 2\dfrac{U^{(3)}}{U^{(1)}} & 0 \\ -\dfrac{U^{(3)}U^{(4)}}{U^{(1)^2}} & 0 & \dfrac{U^{(4)}}{U^{(1)}} & \dfrac{U^{(3)}}{U^{(1)}} \end{bmatrix} = \begin{bmatrix} 0 & 0 & 1 & 0 \\ -uv & v & u & 0 \\ -v^2 & 0 & 2v & 0 \\ -vE & 0 & E & v \end{bmatrix}, \tag{18}$$

which together form the Jacobian tensor

$$\mathbf{A} = \left(\frac{\partial F^{(x)}}{\partial U}, \frac{\partial F^{(y)}}{\partial U} \right). \tag{19}$$

The coupled transport Eq. (13) describe the transport of the conserved quantities U with the velocity $\mathbf{v}$. A spectral analysis of both Jacobians shows that the eigenvalues are given by

$$\lambda^{(x)} = \{u, u, u, u\} \quad \text{and} \quad \lambda^{(y)} = \{v, v, v, v\} \tag{20}$$

for the coordinate directions x and y. Moreover, both spaces of eigenvectors are three dimensional. Hence, the Jacobians are not diagonalizable and the governing equations lack hyperbolicity. Since the eigenvalues $\lambda^{(x)}$ and $\lambda^{(y)}$ represent the characteristic speeds of wave propagation, information travels as a single wave with velocity $\mathbf{v}$.

Furthermore, the homogeneity property

$$F^{(d)}(U) = \frac{\partial F^{(d)}(U)}{\partial U} U, \quad d = x, y, \tag{21}$$

which also is a feature of the Euler equations [34], makes it possible to rewrite the discretization equivalently as a matrix–vector product, and enables the derivation of semi-implicit time stepping schemes without loss of conservation.

Due to the lack of pressure, delta shocks may in principle appear in the particulate phase. They are excluded by the assumption of dilute conditions. In addition, the interface exchange terms also play an important role in preventing such unphysical phenomena, although there is no mathematical proof available. The gas pressure is linked to the velocity in such a way that the gas density remains bounded. Since the velocity of particles is also related to the gas velocity by the magnitude of interfacial drag, the gas pressure influences the velocity of the particles in some sense. This may be a reason why delta shocks are not observed in the particulate phase.

3. Discretization

The construction of the high-resolution scheme basically involves three steps [3]. First, the standard Galerkin discretization serves as a second-order scheme. Since the Galerkin discretization is oscillatory and unstable, we add a suitably defined artificial diffusion operator D to preserve the physical properties of the solution. The error induced by this manipulation is proportional to the mesh size, which reduces the order of approximation to one. For this reason the resulting discretization is called low-order scheme. Finally, we increase the order of approximation by reinserting a limited fraction of nonlinear antidiffusion F^*, which results in the desired high-resolution scheme. The amount of antidiffusion is controlled by TVD-type flux limiters based on the local smoothness of the solution. Note that we compute the stabilization for each phase separately. Hyperbolic solvers can be applied to the equations governing the gas phase, while scalar dissipation is feasible for the pressureless conservation laws of the particulate phase. The design of the artificial diffusion operator for the gas phase can be found in [4,2,9,18]. Therefore it remains to define the stabilization of the particulate phase.

3.1. Second-order scheme

Given a suitable set of continuous linear or bilinear basis functions $\{\varphi_i\}$, let the numerical solution and the convective fluxes be interpolated using the group finite element formulation [35]

$$U_h(\mathbf{x}, t) = \sum_i \varphi_i(\mathbf{x}) U_i(t), \qquad \mathbf{F}_h(\mathbf{x}, t) = \sum_i \varphi_i(\mathbf{x}) \mathbf{F}_i(t), \tag{22}$$

where $\mathbf{F}_i$ is the flux tensor evaluated using the solution values at node i. Multiplying the governing equations (12) by a test function and integrating over the domain, one obtains the Galerkin finite element discretization

$$\sum_j \left[\int_\Omega \varphi_i \varphi_j \, \mathrm{d}\mathbf{x} \right] \frac{\mathrm{d}U_j}{\mathrm{d}t} + \sum_j \left[\int_\Omega \varphi_i \nabla \varphi_j \, \mathrm{d}\mathbf{x} \right] \cdot \mathbf{F}_j = \int_\Omega \varphi_i \tilde{S} \, \mathrm{d}\mathbf{x} \quad \forall i. \tag{23}$$

The latter equation can be written in a shorter form

$$\sum_j M_{ij} \frac{\mathrm{d}U_j}{\mathrm{d}t} = -\sum_j \mathbf{c}_{ij} \cdot \mathbf{F}_j + \int_\Omega \varphi_i \tilde{S} \, \mathrm{d}\mathbf{x}. \tag{24}$$

In the formula above, the $4\,\mathrm{NVT} \times 4\,\mathrm{NVT}$-matrix M_C (NVT = number of vertices) denotes the block consistent mass matrix

$$\{M_{ij}\} = \{m_{ij} I\} = M_C, \tag{25}$$

where I is the 4×4 identity matrix. The coefficients of this finite element scheme are given by

$$m_{ij} = \int_\Omega \varphi_i \varphi_j \, \mathrm{d}\mathbf{x} \qquad \text{and} \qquad \mathbf{c}_{ij} = \int_\Omega \varphi_i \nabla \varphi_j \, \mathrm{d}\mathbf{x}. \tag{26}$$

Eq. (24) corresponds to the standard Galerkin discretization. For the purpose of implementing numerical boundary conditions, it is more convenient to consider the weak formulation

$$\sum_j M_{ij} \frac{\mathrm{d}U_j}{\mathrm{d}t} = \sum_j \mathbf{c}_{ji} \cdot \mathbf{F}_j - \int_{\partial\Omega} \varphi_i \mathbf{F}_h \cdot \mathbf{n} \, \mathrm{d}s + \int_\Omega \varphi_i \tilde{S} \, \mathrm{d}\mathbf{x}, \tag{27}$$

which makes it possible to prescribe boundary conditions in a weak sense [9,18]. In our algorithm, the weak form of the Galerkin discretization (27) serves as the second-order scheme, while the stabilization is still based on (24).

3.1.1. Discretization of source terms

For the space discretization of hyperbolic equations with source terms an upwind approximation of source terms is sometimes proposed, similar to the upwind approximation of hyperbolic terms [36]. A much simpler approach has been successfully used in [16,17,15], where the source terms are discretized in a pointwise way. The accuracy of a pointwise approximation is emphasized in [14]. A similar finite-element-like approximation is proposed in this paper.

A direct integration of the source terms involves numerical integration in each iteration step, which makes the integration very time consuming. To discretize the source terms in a finite-element-like way without numerical integration in each (pseudo) time step, we adopt the group finite element formulation, which was originally defined for hyperbolic terms [35]. Hence, we interpolate the source terms in the space of basis functions

$$\tilde{S}_h = \sum_i \varphi_i \tilde{S}_i, \tag{28}$$

where

$$\tilde{S}_i = \big(0, \quad -\mathbf{F}_{Di}, \quad -\mathbf{v}_{p_i} \cdot \mathbf{F}_{Di} - Q_{Ti}, \quad 0, \quad \mathbf{F}_{Di}, \quad \mathbf{v}_{p_i} \cdot \mathbf{F}_{Di} + Q_{Ti}\big) \tag{29}$$

denotes the source terms evaluated at the corresponding node i. Due to the homogeneity property the discrete transport operator resulting from flux discretization can be expressed by the matrix–vector product KU, which includes the discretized hyperbolic terms and boundary conditions. Substituting (28) into (24) yields semi-discretized equations of the form

$$M_C \frac{\mathrm{d}U}{\mathrm{d}t} = KU + M_C S \tag{30}$$

due to the homogeneity property. At the same time, one replaces the consistent mass matrix by its lumped counterpart, which transforms (30) to

$$M_L \frac{\mathrm{d}U}{\mathrm{d}t} = KU + M_L S. \tag{31}$$

This type of source term discretization is closely related to the finite volume framework, and the source term integration by schemes which take advantage of operator splitting. The replacement of the consistent mass matrix with the lumped one enables a pointwise updating strategy in an operator splitting approach. Moreover, the lumped mass matrix prevents the birth of oscillations due to nonzero off-diagonal source term blocks. Such treatment of source terms is also feasible in a fully coupled approach, which is favored in this work since it does not violate the physical properties of the solution. It is a well known fact that the two-fluid equations do not conserve momentum and energy of each phase separately, in contrast to the mixture momentum and energy which are perfectly conserved. Eq. (31) clearly features this property. Furthermore, the positivity constraint is not affected by the source terms nor are numerical oscillations observed in the computational results.

3.2. Low-order scheme and algebraic flux correction

In this section we focus on the stabilization of the convective fluxes related to the particulate phase and we neglect the gas phase as well as the algebraic source terms for convenience. The process of algebraic flux correction begins with row-sum mass lumping on the left hand side of the semi-discrete Galerkin scheme

$$M_L \frac{\mathrm{d}U}{\mathrm{d}t} = KU. \tag{32}$$

The lumped counterpart of the consistent mass matrix M_C is given by

$$M_L = \mathrm{diag}\{M_i\}, \quad M_i = m_i I, \text{ and } m_i = \sum_j m_{ij}. \tag{33}$$

Note that mass lumping related to the time derivative does not affect the accuracy since the time derivative vanishes in the stationary limit, while it improves the matrix properties and the performance of iterative linear solvers.

The lack of hyperbolicity rules out the usual approach in construction of approximate Riemann solvers, which is based on edge-by-edge transformations to local characteristic variables. In the case of the pressureless particle equations, such transformations are neither possible nor necessary. Since there exists just one wave moving with the flow velocity $\mathbf{v}$, stabilization by scalar dissipation defined in terms of the conservative variables is feasible. Since the same diffusion coefficient applies to each equation, the lack of hyperbolicity turns out to be an advantage rather than a drawback as far as stabilization is concerned. The discrete transport coefficients

$$k_{ij} = -\mathbf{c}_{ij} \cdot \mathbf{v}_j \tag{34}$$

are defined as in the case of scalar transport equations [3], and the artificial diffusion coefficients d_{ij} have the same value for all conservative variables. The default setting

$$d_{ij} = \max\{-k_{ij}, 0, -k_{ji}\} = d_{ji} \tag{35}$$

as stated in [3], is sufficient to satisfy the scalar LED criterion [3]. However, the theoretical framework is invalid for nonlinear coupled systems. Therefore, a low-order scheme based on (35) may produce undershoots and overshoots that carry over to the flux-limited solution. It turns out that a slightly increased amount of diffusion is sufficient to get rid of non-physical oscillations and compute a physically correct Riemann solution. An algebraic analysis of the Rusanov-type scheme presented by Banks and Shadid [37] leads to the following revised definition

$$d_{ij} = \max\{|k_{ij}|, |k_{ji}|\} = d_{ji}. \tag{36}$$

The resulting low-order scheme is more diffusive than that based on (35). Indeed,

$$\max\{|k_{ij}|, |k_{ji}|\} \geq \max\{-k_{ij}, 0, -k_{ji}\}. \tag{37}$$

As before, the contribution of the artificial diffusion operator to the modified Galerkin scheme can be decomposed into a sum of numerical fluxes. In vectorial notation this looks like

$$F_{ij}^{\mathrm{diff}} = |\Lambda_{ij}|(U_j - U_i), \qquad F_{ji}^{\mathrm{diff}} = -F_{ij}^{\mathrm{diff}}, \tag{38}$$

where

$$|\Lambda_{ij}| = \mathrm{diag}\{d_{ij}, d_{ij}, d_{ij}, d_{ij}\} = d_{ij} I \tag{39}$$

is a diagonal matrix of diffusion coefficients.

The construction of the low-order scheme is followed by a nonlinear antidiffusive correction. As in the case of scalar equations, the amount of antidiffusion must be limited, so as to keep the scheme non-oscillatory. The correction factors are computed for each equation separately. The only difference is the new formula (36) for the artificial diffusion coefficient. The pair of limited antidiffusive fluxes associated with nodes i and j is of the form

$$F_{ij}^{*} = |\Lambda_{ij}^{*}|(U_i - U_j), \qquad F_{ji}^{*} = -F_{ij}^{*}, \tag{40}$$

where

$$|\Lambda_{ij}^{*}| = \mathrm{diag}\{\beta_{ij}^{(1)} d_{ij}, \beta_{ij}^{(2)} d_{ij}, \beta_{ij}^{(3)} d_{ij}, \beta_{ij}^{(4)} d_{ij}\} \tag{41}$$

is a limited counterpart of $|\Lambda_{ij}|$. Since the coupling is rather weak, the solution-dependent correction factors β_{ij} are chosen individually for each equation. This is due to the fact that there is just one wave and, consequently, just one characteristic direction in which the wave can travel. An algorithm for the determination of the correction factors can be found in [1]. This algorithm is applied separately to each of the equations modeling the particulate phase.

Although algebraic flux correction for the equations of the particulate phase is performed in a segregated fashion, the resulting algebraic system should be solved in a fully coupled way. Decoupled solution strategies may require less memory but give rise to additional time step restrictions. Moreover, intermediate solutions are more likely to exhibit numerical oscillations that inhibit convergence to steady state. Those strategies typically involve successive solution of a sequence of subproblems and demand the use of out-dated quantities. The result is an inaccurate stabilization as long as the solution has not converged. In the steady-state limit this problem vanishes since the solution will no longer change significantly. Nevertheless, convergence can only be reached for small time steps since inaccurate stabilization due to large time steps will prevent convergence. Therefore, the development of strongly coupled iterative solvers for flux-limited Galerkin discretizations constitutes a major highlight of the present study. The implementation of two-way coupling mechanisms, implicit time integration schemes, and Newton-like methods for nonlinear algebraic systems is described in the following chapters.

4. Boundary conditions

The two-fluid model consists of the Euler equations written in terms of the effective density and the pressureless transport equations. These subproblems are linked by algebraic source terms. The flux Jacobians of the coupled system lack diagonalizability since an incomplete set of seven independent eigenvectors exists. Therefore, it is neither possible nor necessary to prescribe characteristic boundary conditions for the coupled two-fluid equations. As a matter of fact, it suffices to implement boundary conditions for the equations governing each phase separately.

Both phases involve similar boundary integrals. Therefore, the computation of the boundary integral is exactly the same for both phases, but the treatment of the boundary fluxes differs. The Euler equations admit three waves moving at different speeds and in different directions, which necessitates the specification of characteristic boundary values in terms of the Riemann invariants. In contrast, the equations modeling the particulate phase only admit one wave moving with the fluid velocity. Hence, the whole information propagates with the particle velocity. This enables the specification of boundary values in terms of conservative variables rather than Riemann invariants.

It was already shown in [9,18] that weak Neumann-type flux boundary conditions are much more robust than their strongly impost counterparts. The accuracy was also emphasized in the references cited above. In this study we prescribe weak Neumann-type flux boundary conditions. To impose boundary conditions of that type we only manipulate the boundary fluxes in the boundary integrals so as to satisfy the boundary conditions.

4.1. Inlet and outlet boundary conditions

Without loss of generality we assume that

$$v_{p,n}\, v_{g,n} > 0, \tag{42}$$

where $v_{p,n} = \mathbf{n} \cdot \mathbf{v}_p$ and $v_{g,n} = \mathbf{n} \cdot \mathbf{v}_g$ are the normal velocities of the particles and gas, respectively. In other words, the case that one phase enters the domain while the other phase leaves the domain simultaneously is excluded from the scope of this paper. Note that this simplifies notation, but does not limit the computational scheme.

A part of the boundary is called inlet if the normal velocities of both phases satisfy

$$v_{p,n} < 0 \quad \text{and} \quad v_{g,n} < 0, \tag{43}$$

otherwise it is referred to as an outlet. Inlet and outlet boundary conditions for the gas phase are the same as described in [9, 18] for the effective density $\rho = \alpha_g \rho_g$ and it suffices to discuss boundary conditions for the particulate phase in the present section. Consequently, the inflow and outflow can be subsonic or supersonic depending on the Mach number. In contrast, the wave of the particulate phase enters the domain at an inlet, which requires the specification of the complete vector of conservative variables. At an outlet, the wave leaves the domain and no information has to be prescribed. To simplify notation, the index denoting the particulate phase is neglected in the following formulas.

The restriction to one wave simplifies the solution of the boundary Riemann problem of the particulate phase. To avoid unphysical boundary layers [38], we use the same boundary Riemann solver as for the gas phase [38,9]. The flux formula of Roe is given by

$$\mathbf{n} \cdot \tilde{\mathbf{F}}_h = F(U_i, U_\infty) = \frac{1}{2}\mathbf{n} \cdot (\mathbf{F}(U_i) + \mathbf{F}(U_\infty)) - \frac{1}{2}|A_{i\infty}^{n}|(U_\infty - U_i) \tag{44}$$

with the flux tensor $\mathbf{F}$ defined by (16). Due to scalar dissipation the matrix $|A^n_{i\infty}|$ exhibits a diagonal structure

$$|A^n_{i\infty}| = \operatorname{diag}\{d_{i\infty}, d_{i\infty}, d_{i\infty}, d_{i\infty}\}, \quad d_{i\infty} = \max\{|\mathbf{n}\cdot\mathbf{v}_i|, |\mathbf{n}\cdot\mathbf{v}_\infty|\} \tag{45}$$

in contrast to its counterpart corresponding to the Euler equations. This is similar to the scalar upwind formulation of each equation. In order to clarify the last statement, let us consider a local linearization of the characteristic speed

$$\hat{v} = \begin{cases} \mathbf{v}_i\cdot\mathbf{n} & \text{if } \mathbf{v}_i\cdot\mathbf{n} \geq 0 \\ \mathbf{v}_\infty\cdot\mathbf{n} & \text{if } \mathbf{v}_i\cdot\mathbf{n} < 0 \end{cases} \tag{46}$$

of the particulate phase. Due to this assumption, the boundary flux is given by (the non-conservative formulation)

$$\begin{aligned} F_{\text{lin}}(U_i, U_\infty) &= \frac{\hat{v}}{2}(U_i + U_\infty) - \frac{\hat{v}}{2}(U_\infty - U_i) \\ &= \frac{\hat{v} + |\hat{v}|}{2}U_i + \frac{\hat{v} - |\hat{v}|}{2}U_\infty \\ &= \begin{cases} U_i\hat{v} & \text{if } \hat{v} \geq 0 \\ U_\infty\hat{v} & \text{if } \hat{v} < 0 \end{cases} \end{aligned} \tag{47}$$

and is clearly equivalent to the one-dimensional upwind approximation. The boundary flux (44) provides a quite similar treatment, where $d_{i\infty}$, given by Eq. (45), mimics an approximation of the characteristic speed, which is consistent with the inner discretization. Considering the last arguments it is sufficient to define the ghost state by the values of the interior state in the case of an outlet or by the imposed boundary condition at an inflow part of the boundary.

4.2. Wall boundary conditions

The wall boundary condition

$$v_{p,n} = 0 \tag{48}$$

should also be imposed on the equations governing the particulate phase. Since they do not involve a pressure gradient in contrast to the Euler equations, it is insufficient to apply the concepts developed for the Euler equations [9,18]. The wall boundary condition cannot be enforced just by canceling the boundary integral arising from the Galerkin discretization. Such an implementation does not inhibit fluxes penetrating through the walls. In the case of the Euler equations the nonzero pressure serves as a kind of source term, which prevents nonzero normal fluxes. Due to the lack of pressure the volume integrals may become large in comparison with the boundary integrals, which may also be a reason for the penetration of particles through the wall.

A simple way to circumvent this problem is to enforce flow tangency after each iteration by subtracting the normal components of the momentum equations

$$(K^*U)_i = (K^*U)_i - \left((K^*U)_i \cdot \begin{bmatrix} 0 \\ \mathbf{n}_i \\ 0 \end{bmatrix}\right) \begin{bmatrix} 0 \\ \mathbf{n}_i \\ 0 \end{bmatrix} \tag{49}$$

at any wall boundary node i in a strong sense. This conflicts with the boundary conditions imposed on the gas phase and gives rise to spurious boundary layers due to the inconsistent wall boundary treatment of both phases. On the other hand, the weak implementation of boundary conditions provides superior robustness, faster convergence, and accuracy in steady-state computations.

We therefore add an additional penalty term to the weak form of the momentum equations of both phases

$$\text{penalty} := -\sigma \int_{\Gamma_{\text{wall}}} \omega |v_n| \rho^2 v_n \mathbf{n}\, \mathrm{d}s, \tag{50}$$

where $\sigma \gg 1$ is a large positive penalty parameter and ω represents the test function. The integration is carried out over the wall boundary and the penalty term, which appears on the right hand sides of the momentum equations, is set to zero elsewhere. Penalty terms were successfully applied to the incompressible Navier–Stokes equations [39] and reactive bubbly flows [22]. For the Euler equations a penalty term very similar to (50) was proposed in [40] to enforce the wall boundary condition. A more theoretical analysis of penalty techniques can be found in [41,42]. Moreover, the performance of those terms in the framework of (scalar) transport equations as well as the incompressible Navier–Stokes equations was established in [43]. Although the free-slip condition can be prescribed much easier for the gaseous phase, the particle equations require such a penalty term. It is also added to the gas momentum equations to equalize the treatment of both phases and to avoid boundary layers, which may arise due to different boundary implementations. Nevertheless, the no-penetration condition

$$\mathbf{v}\cdot\mathbf{n} = 0 \tag{51}$$

can be substituted into the boundary integrals of each phase. Due to this fact, the boundary integrals of the particle equations related to solid walls vanish and the corresponding terms of the gas equations simplify to

$$\mathbf{n}\cdot\tilde{\mathbf{F}}_{h|_{\text{wall}}} = \begin{bmatrix} 0 \\ n^{(x)}P \\ n^{(y)}P \\ 0 \end{bmatrix}. \tag{52}$$

Obviously, any weak solution of the governing equations also satisfies the modified equations with the additional penalty term. On the other hand, a weak solution of the modified equations satisfies the free-slip condition as well as the governing equations since convergence forces the penalty term to vanish and the free-slip condition to be satisfied.

The penalty term turns out to be very large and stiff due to the large penalty parameter σ. This gives rise to rather large errors in the early stages of a simulation since the free-slip condition is usually not yet satisfied initially. Care must therefore be taken in the design of the preconditioner to achieve convergence. Note that the sign of the penalty term is chosen to restrict the contribution to the preconditioner positive semi-definite [9] so as to improve its matrix properties [40]. Additionally, the abrupt change in the normal velocity due to an initial solution violating the free-slip condition may cause divergence. This is not a drawback of the penalty term, the problem is caused by physical reasons since such an impulsive start is physically impossible [44]. The initially large errors decrease significantly by several orders of magnitude during a few iterations since the normal velocity vanishes after a few iteration steps. However, a converged solution does not depend on the way it was computed. Therefore, one may start the simulation with a small penalty parameter and increase it during the first iterations. Such a procedure is closely related to the underrelaxation of the wall boundary condition proposed by Lyra [44]. Note that the penalty term is also applicable to transient computations since the initial solution satisfies the wall boundary condition for the physical reasons pointed out above.

5. Time integration

The source terms introduce a two-way coupling and give rise to an additional nonlinearity in the model. The presence of small particles causes the source terms relating to the drag force and heat exchange to dominate. This in turn leads to slow convergence when using implicit solvers and aggravates the already very restrictive stability constraints in explicit computations. To circumvent this problem, source terms are usually included into the two-fluid model by way of operator splitting; see among others [16,17,15]. In this paper we propose a fully coupled semi-implicit algorithm, where both the discretized fluxes and source terms are treated in a semi-implicit way by a Newton-like method. This turns out to be much more robust and stable in practical applications than the schemes, which rely on operator splitting.

5.1. Operator splitting

The operator splitting approach makes it possible to develop independent solvers for both the hyperbolic terms and the source terms. In such an approach, the hyperbolic terms are usually discretized using explicit methods developed in the framework of single-phase equations. On the other hand the source terms call for an implicit solver due to their stiffness. At the same time, they can be integrated by a semi-analytical way [17,45].

In the references cited above the Yanenko splitting of first-order accuracy is employed since it removes the source terms and therefore the associated stability constraints completely from the equations accounting for the hyperbolic terms. The computation of the transport terms is the most time and memory consuming part of the simulation of these types of multi-phase flows. Operator splitting techniques seem to be promising methods since they make it possible to solve for the hyperbolic terms of both phases separately even for implicit approaches. In transient computations this completely holds true, while operator splitting techniques are less efficient or even less accurate in steady-state computations. Although some splitting techniques are unconditionally stable, they typically do not allow the solution to approach steady state for moderate and large CFL numbers.

For the (pseudo) time integration of (4) one may apply operator splitting to circumvent the convergence and stability problems associated with the nonlinearity induced by the source terms. As a starting point, we recall the operator splitting that was applied to the two-fluid model in [38]. In transient computations a time integration scheme of second or higher order is usually applied. To preserve the overall accuracy in time-dependent computations, the use of second- or higher-order operator splitting schemes is required. Since this study focuses on stationary solutions, first-order splitting techniques combined with backward Euler time stepping suffice for this purpose. The hyperbolic terms are linearized for our computations as described below.

5.1.1. Yanenko splitting

A popular approach is the Yanenko splitting [17,45,15]

$$\frac{U^* - U^n}{\Delta t} + \nabla\cdot\mathbf{F}^* = 0 \tag{53}$$

$$\frac{U^{n+1}-U^*}{\Delta t}=S^{n+1}, \tag{54}$$

where the superscript n denotes the time level. In the first step, the numerical solution is advanced in time without taking the source terms into account. In the second step, the nodal values of the resulting solution U^* are corrected by adding the contribution of S^{n+1}.

For an explicit solver fitted to transient simulations, the Yanenko splitting is a good choice, although it is only first-order accurate. It turns out to be very robust and to be applicable to nearly arbitrary CFL numbers. After the first step (53) the source term step (54) changes the intermediate solution U^* depending on the length of the time step, so that the final solution U^{n+1} does not satisfy the equations of the first subproblem. The solution will actually not approach steady state since it depends on the length of the time step. The Yanenko splitting is therefore restricted to time-dependent flows and very small time steps.

5.1.2. Douglas–Rachford splitting

To make sure that the splitting does not disturb solutions approaching a steady state, we replace (53)–(54) by the Douglas–Rachford scheme [46]

$$\frac{U^*-U^n}{\Delta t}+\nabla\cdot\mathbf{F}^*=S^n \tag{55}$$

$$\frac{U^{n+1}-U^*}{\Delta t}=S^{n+1}-S^n, \tag{56}$$

which is known to be very robust, at least in the context of alternating direction implicit (ADI) iterative solvers for multidimensional problems.

The implicit correction in the second step does not change a converged stationary solution and allows the solution to approach steady state. The density of the particulate phase is constant, while its volumetric fraction is variable. This is another reason why the Douglas–Rachford splitting is preferred to the Yanenko splitting. Due to the above mentioned drawbacks of the Yanenko splitting, the Douglas–Rachford splitting is employed in this paper.

Let us focus our attention on the second step (56) of the Douglas–Rachford splitting since the first step (55) corresponds to the hyperbolic solver, which is described in Section 5.2. It is followed by an implicit correction of the involved interface transfer terms. In this step, the drag force and heat exchange terms are discretized in a semi-implicit fashion. First, the velocities are updated by solving the linear system

$$(\alpha_p\rho_p)^*\,\frac{\mathbf{v}_p^{n+1}-\mathbf{v}_p^*}{\Delta t}=\gamma_D^*(\mathbf{v}_g^{n+1}-\mathbf{v}_p^{n+1})-\mathbf{F}_D^n \tag{57}$$

$$(\alpha_g\rho_g)^*\,\frac{\mathbf{v}_g^{n+1}-\mathbf{v}_g^*}{\Delta t}=\gamma_D^*(\mathbf{v}_p^{n+1}-\mathbf{v}_g^{n+1})+\mathbf{F}_D^n, \tag{58}$$

where the superscript $*$ refers to the solution of system (55) and

$$\gamma_D^*=\frac{3}{4}C_D^*\frac{\rho_g^*}{d}\alpha_p^*|\mathbf{v}_g^*-\mathbf{v}_p^*|. \tag{59}$$

Once the velocities have been updated, the changes in energy due to the interfacial drag and heat exchange are taken into account as follows:

$$(\alpha_p\rho_p)^*\frac{E_p^{n+1}-E_p^*}{\Delta t}=\gamma_T^*(T_g^{n+1}-T_p^{n+1})-\tilde{Q}_T^n \tag{60}$$

$$(\alpha_g\rho_g)^*\frac{E_g^{n+1}-E_g^*}{\Delta t}=\gamma_T^*(T_p^{n+1}-T_g^{n+1})+\tilde{Q}_T^n. \tag{61}$$

The heat transfer coefficient γ_T^* and net source/sink $\tilde{Q}_T^n$ are given by

$$\gamma_T^*=\frac{\mathrm{Nu}^*6\kappa_g}{d^2}\alpha_p^*,\qquad \tilde{Q}_T^n=Q_T^n+\mathbf{v}_p^{n+1}\cdot\mathbf{F}_D^{n+1}-\mathbf{v}_p^n\cdot\mathbf{F}_D^n. \tag{62}$$

Since mass transfer does not take place, there are no source terms in the continuity equations. Therefore, the effective densities $(\alpha\rho)_k^{n+1}:=(\alpha\rho)_k^*$ remain unchanged.

Numerical experiments indicate that steady-state convergence of the Douglas–Rachford splitting can only be achieved for small CFL numbers. It is a well-known fact that decoupled solution strategies are unfavorable in steady-state computations due to their time step restrictions. In practice one has to make a decision in the trade-off between the low computational costs of segregated algorithms in comparison with strongly coupled methods and the much more restrictive time step constraints of the former family of methods. An implicit time stepping scheme without use of operator splitting, which offers the potential of unconditional stability and convergence, is preferable in steady-state simulations and is therefore developed in this study.

5.2. The fully coupled solver

It is common practice to solve the arising nonlinear systems by pseudo time stepping schemes for marching the solution to steady state. The time step can be interpreted as an underrelaxation, where a time step of infinite length corresponds to a direct solution of the stationary equations without underrelaxation. In this study we employ the backward Euler scheme to integrate the fluxes and source terms. We will demonstrate in Section 6.3 by numerical results that a fully coupled solution strategy is much more robust then operator splitting based approaches. Therefore, the governing equations are solved in a fully coupled way, although the stabilization was defined for each phase individually. To avoid computationally expensive nonlinear iterations, the fluxes and source terms are linearized by a Taylor series expansion.

5.2.1. Linearized backward Euler scheme

The spatially discretized two-fluid model can be expressed in the condensed form

$$M_L \frac{\mathrm{d}U}{\mathrm{d}t} = F + S, \tag{63}$$

where U is the vector of conservative variables, F is the flux vector, and S represents the source terms of the two-fluid model. This system of ordinary differential equations can be integrated in time by the backward Euler scheme

$$M_L \frac{U^{n+1} - U^n}{\Delta t} = F^{n+1} + S^{n+1} \tag{64}$$

with a time step of length Δt. The superscript n refers to time level n and the result is a nonlinear system of algebraic equations, which calls for nonlinear iterations in each (pseudo) time step. Nonlinear iterations are computationally very expensive. To circumvent this problem, one assumes sufficient smoothness and linearizes the equations around the current solution U^n by a Taylor series expansion of the fluxes

$$F^{n+1} = F^n + \left(\frac{\partial F}{\partial U}\right)^n (U^{n+1} - U^n) + \mathcal{O}(\|U^{n+1} - U^n\|^2) \tag{65}$$

and the source terms

$$S^{n+1} = S^n + \left(\frac{\partial S}{\partial U}\right)^n (U^{n+1} - U^n) + \mathcal{O}(\|U^{n+1} - U^n\|^2). \tag{66}$$

Substitution of Eqs. (65) and (66) into the nonlinear equation (64) leads to a linear algebraic system

$$\left[\frac{M_L}{\Delta t} - \left(\frac{\partial F}{\partial U} + \frac{\partial S}{\partial U}\right)^n\right] (U^{n+1} - U^n) = F^n + S^n. \tag{67}$$

Due to the linearizations (65) and (66) the latter scheme is time accurate of first order and applicable to stationary as well as transient flows, although a time integration scheme for transient flows should be at least second-order accurate. Furthermore, nonlinear iterations are avoided and merely a linear system of algebraic equations has to be solved at each time level. Note that due to the homogeneity property the semi-implicit time marching scheme remains conservative, even if it is applied to transient problems.

At first glance, this scheme seems to be conditionally stable since it is semi-implicit. On the other hand, there is strong numerical evidence that the semi-implicit scheme based on the backward Euler method is unconditionally stable if the initial values are sufficiently accurate.

Suppose that both the fluxes and the source terms are differentiable with respect to the conservative variables. Setting the time step (or the CFL number) of the semi-implicit time stepping scheme to infinity, one recovers Newton's method

$$-\left(\frac{\partial F}{\partial U} + \frac{\partial S}{\partial U}\right)^n (U^{n+1} - U^n) = F^n + S^n, \tag{68}$$

which is known to have second order of convergence (quadratic convergence) under these conditions. Corresponding to the notation used in this paper, Newton's scheme is also denoted by CFL $= \infty$, which is related to a time step of infinite length.

It is a well-known fact that the convergence of Newton's method depends on a sufficiently accurate initial state. The Taylor linearization is only valid in a vicinity of the current solution U^n. This is the reason, why a suitable initial guess is essential. Note that this requirement is not a stability restriction and the time step can actually be arbitrarily large. The only condition is that the solution does not change rapidly at each time level. To satisfy this constraint and make the linearization valid, either small time steps or a suitable initial guess are crucial. For the computations reported below we did a few pre-iterations with CFL $=$ 10. After the algorithm starts converging one can increase the CFL number to an arbitrarily large or infinite value. Since the computation of the original Jacobian matrix is a complicated task and may worsen the matrix properties, a low-order approximation of the Jacobian will serve as a preconditioner. To indicate this fact, the scheme will be called Newton-like. The approximation does not provide second-order convergence, but yields a robust and parameter-free

scheme. There is no significant loss of efficiency since second-order convergence is related to differentiability of the residual, which is not available for the flux function of Roe and the limiter function applied in this study.

The linear systems arising by (67) and (68) are solved by the BiCGSTAB method combined with an ILU preconditioner. In our computations the linear iterations were stopped after the residual decreased by three orders of magnitude.

There are several possibilities to approximate the Jacobian. Some of them are sketched in [9]. In this study we employ approximations of the flux and source term Jacobians, which can be assembled cheaply and provide very good matrix properties.

5.2.2. Edge-based approximate interior flux Jacobian

The original flux Jacobian in (67) and (68) is replaced by an edge-based approximation of the low-order Jacobian, where the correction factors are neglected. The approximate Jacobian (or preconditioner) constructed in this way is free of additional problem-dependent parameters and enjoys several advantages in comparison with the previously discussed approximations. No additional fill-in is created since the low-order fluxes only depend on the direct neighbors of a current node. For scheme (67) the resultant matrix is of M-matrix type, which is related to positivity preservation of each iterate subject to a suitable time step (at least on the characteristic level). This is an important fact since it rules out unphysical effects, which may cause divergence (e.g. zero density). The low-order approximation therefore provides increased robustness and is subject to lower memory requirements. Moreover, its computation is much less expensive than that of the approximation of the full Jacobian.

The kind of Jacobian approximation proposed here can be determined analytically by a derivation of the low-order fluxes under certain simplifying assumptions. The sum of fluxes into a node i, which is related to the ith row of the residual vector, is given by

$$F_i^{\text{low}} = \sum_j \mathbf{c}_{ji} \cdot \mathbf{F}_j - \underbrace{\int_{\partial\Omega} \varphi_i \mathbf{n} \cdot \mathbf{F}_h \, \mathrm{d}s}_{=B_i} + \sum_{j \neq i} D_{ij}(U_j - U_i). \tag{69}$$

On the right hand side the first three terms represent the Galerkin discretization (27) and the discretized source terms. For the gaseous phase of the two-fluid model D_{ij} are the diffusion blocks defined in [9,2,4,18]. In the case of the particulate phase D_{ij} can be written as

$$D_{ij} = \text{diag}\{d_{ij}, d_{ij}, d_{ij}, d_{ij}\}, \tag{70}$$

where d_{ij} are given by (36). For the sake of simplicity one assumes that the diffusion blocks are constant with respect to the conservative variables. The first term of Eq. (69) involves the Galerkin coefficients $\mathbf{c}_{ji}$ defined by (26). They are independent of the conservative variables. Under the above simplification, the derivatives of the low-order nodal flux F_i^{low} with respect to the conservative variables at nodes i and j are given by

$$\frac{\partial F_i^{\text{low}}}{\partial U_j} = \mathbf{c}_{ji} \cdot \mathbf{A}_j - \frac{\partial B_i}{\partial U_j} + D_{ij}, \qquad \frac{\partial F_i^{\text{low}}}{\partial U_i} = \mathbf{c}_{ii} \cdot \mathbf{A}_i - \frac{\partial B_i}{\partial U_i} - \sum_{j \neq i} D_{ij} \tag{71}$$

where $\mathbf{A}_j$ and $\mathbf{A}_i$ is the Jacobian tensor evaluated at nodes j and i, respectively. The approximate Jacobian proposed so far is exact with respect to the Galerkin discretization if the derivative of the boundary part and the source terms can be determined exactly. The derivation of the boundary integral B_i is complicated since the solution of the boundary Riemann problem is involved and the ghost state may even depend on its related interior counterpart. We refer the interested reader to [9], where a boundary flux Jacobian is derived by multiple applications of the chain rule.

The approximation of the source term Jacobian is also a delicate task since the source terms are rather stiff and dominating. They should be treated implicitly and a suitable approximation of the Jacobian is required. On the other hand the source terms lack smoothness and the Jacobian does not exist analytically. In [9] approximate drag force and heat exchange Jacobians are derived by treating the non-smooth parts as constants. These Jacobians are used in the present study.

6. Numerical results

The performance of the developed numerical scheme has been verified for the Euler equations and a superior robustness and convergence of the weak boundary conditions was shown numerically [9,18]. In this section we focus on the analysis of the two-fluid model featuring a two-way coupling. The first goal of this chapter is to validate the code and compare with benchmark computations from the literature. At the same time it is shown that the discretization of the two-fluid model features most of the properties of the single-phase gas code. The nonlinear convergence analysis is therefore another important goal. It follows from the numerical results that the nonlinear convergence behavior is qualitatively comparable to the single-phase gas computations. The rate of nonlinear convergence improves with increasing CFL number. The CFL number is defined by

$$\text{CFL} = \lambda_{\max} \frac{\Delta t}{h}, \tag{72}$$

Table 1
Physical constants.

Constant	Value	Unit
γ	1.4	
Pr	0.75	
μ	$2.76 \cdot 10^{-5}$	$\frac{\text{kg}}{\text{m}\cdot\text{s}}$
ρ_p	4000	$\frac{\text{kg}}{\text{m}^3}$
c_{pg}	1040	$\frac{\text{J}}{\text{kg}\cdot\text{K}}$
c_{vg}	743	$\frac{\text{J}}{\text{kg}\cdot\text{K}}$
c_{vp}	1380	$\frac{\text{J}}{\text{kg}\cdot\text{K}}$

Table 2
Mesh properties JPL nozzle.

Level	NVT	NEL
1	182	277
2	640	1 108
3	2387	4 432
4	9205	17 728

where $\lambda_{\max}$ corresponds to the maximum wave speed and h is the spatial length scale. In spite of two conflicting non-differentiable nonlinearities, which act together in the case of the high-resolution scheme, the solution approaches steady state in all computations. One can observe both a genuine unconditional stability and a high and stable convergence rate for very large or even infinite CFL numbers. The performance is highlighted for low Mach numbers and complex flow situations.

In the present chapter two test cases are studied. First the flow in a jet propulsion nozzle (JPL nozzle) is investigated. This test case is characterized by subsonic flow at low Mach numbers in the converging part of the nozzle, which is accelerated up to the supersonic regime. We analyze the nonlinear convergence for both the low-order and the high-resolution scheme. Special attention is also paid to the influence of different mass fractions on the physics of both phases. The second computation deals with the reflection of a stationary shock wave at a ramp under purely supersonic conditions. Based on these computations, we study the effect of different particle sizes and mass fractions.

Both test cases involve the flow of nitrogen laden with small ceramic Al_2O_3 particles. The constants associated with such flow conditions are listed in Table 1. At the inlet a chamber with a homogeneous mixture of uniformly distributed gas and particles is assumed. The temperatures and velocities are in equilibrium. Let us characterize the flow further by the mass fraction

$$\phi = \frac{\alpha_p \rho_p}{\alpha_p \rho_p + \alpha_g \rho_g} \tag{73}$$

to measure the amount of particles in the chamber. In all computations reported below, the penalty parameter is set to $\sigma = 10^8$. Moreover, the high-resolution scheme is always initialized by the low-order solution, which is a sufficiently accurate estimate to render the linearization adequate.

6.1. Jet propulsion nozzle flow

The converging diverging nozzle is characterized by the presence of curved boundaries, a quite steep entrance of 45°, and a relatively thin throat, which results in the large acceleration from Mach number $M = 0.1$ at the inlet up to Mach number $M = 2$ (depending on the mass fraction). Therefore, a large characteristic stiffness arises.

The geometry of the nozzle is adopted from [26], where the upper and lower boundaries serve as solid walls. The left and right boundaries correspond to the inlet and outlet of the domain, respectively. At the subsonic inlet, the free stream conditions from Table 3 are prescribed in contrast to the supersonic outlet, where no boundary condition is needed. The domain is covered by an unstructured triangular coarse grid, which is refined several times for the simulations. The mesh properties at different levels are depicted in Table 2. Computations for various mass fractions are performed to assess the influence on the gas phase and to compare the results with data reported in the literature. First we compute five solutions with $\phi = 0.0$ (pure gas), 0.1, 0.5 and $d = 1\ \mu\text{m}$, $20\ \mu\text{m}$ on mesh level four. For comparison Fig. 1 displays the properties of a pure gas flow. Fig. 2 illustrates the Mach number distribution for the different mass fractions and particle diameters.

We observe that the influence of the particles on the gas Mach number increases with increasing mass fraction. The interfacial area and the amount of drag increase due to larger volume fractions at higher mass fractions, which decelerates the gas and decreases the Mach number. This physical argumentation is clearly confirmed by the numerical solutions, see Figs. 2 and 1 (a). The results are in a good qualitative agreement with the observations of Nishida and Ishimaru [24] and Chang [29], although the configurations are not exactly equivalent.

Despite a much higher volume fraction of up to 50% of the larger particles at the centerline downstream and in the throat, compare Fig. 3(b), the gas Mach number is approximately the same or even slightly higher (at the throat) than in

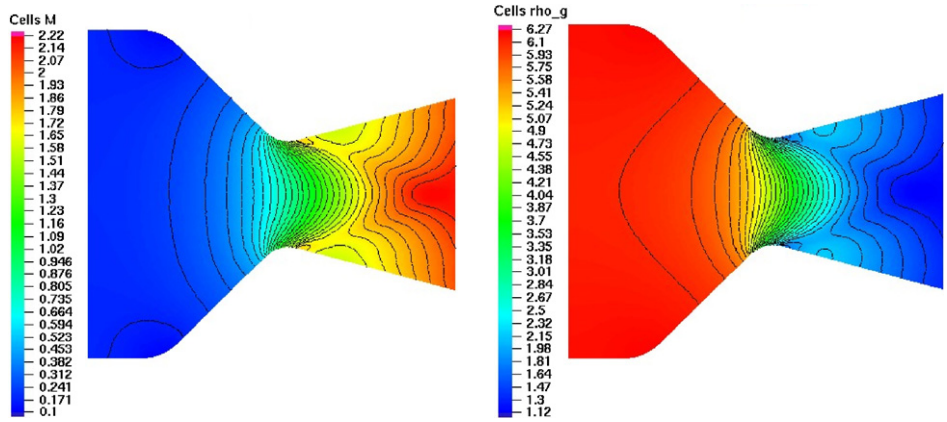

(a) Mach number (blue = 0.1, red = 2.22).

(b) Density (blue = 1.1, red = 6.27).

(c) Temperature (blue = 283, red = 562).

Fig. 1. JPL nozzle: Pure gas flow physics (30 contours). Density in $\frac{\text{kg}}{\text{m}^3}$, temperature in K. (For interpretation of the references to colour in this figure legend, the reader is referred to the web version of this article.)

Table 3
Free stream conditions of the JPL nozzle flow.

Quantity	Value	Unit
M_∞	0.2	
ρ_∞	6.0708	$\frac{\text{kg}}{\text{m}^3}$
P_∞	10^6	Pa
$\mathbf{v}_\infty$	$\sqrt{\frac{\gamma P_\infty}{\rho_\infty}}\begin{pmatrix} M_\infty \\ 0 \end{pmatrix}$	$\frac{\text{m}}{\text{s}}$
ϕ	0.1, 0.5	

the flow laden with smaller particles (see Fig. 3(a)). At first glance this looks surprising. The interfacial area of the flow with $d = 20\ \mu\text{m}$ is indeed smaller than the corresponding interfacial area of the flow laden with particles of diameter $d = 1\ \mu\text{m}$ (for the same volume fraction). Therefore, the magnitude of interfacial drag increases with decreasing particle diameter. Hence, smaller particles are more capable of decelerating the gas than their larger counterparts, which compensates the different magnitude of the volume fractions of both flows. A Mach number increase for larger particles was also observed in [29].

The particle distributions for the mass fraction under consideration, and particle diameters of $d = 1\ \mu\text{m}$, $20\ \mu\text{m}$ can be compared in Fig. 4. A comparison of the two different particle diameters indicates a particle clustering at the walls in the converging part of the nozzle for $d = 20\ \mu\text{m}$. In contrast to the gas phase, the particle velocity is not linked to a pressure term by a constitutive equation, which inhibits such a clustering. The particulate phase is only coupled to the gas pressure by the interfacial forces. A larger particle diameter results in less drag and temperature exchange (for the same volume fraction) due to the smaller interfacial area. Therefore, larger particles are less influenced by the gas than smaller ones, which more or less mimic the gas behavior. The larger particles are therefore less deflected to the centerline by the gas flow, or more

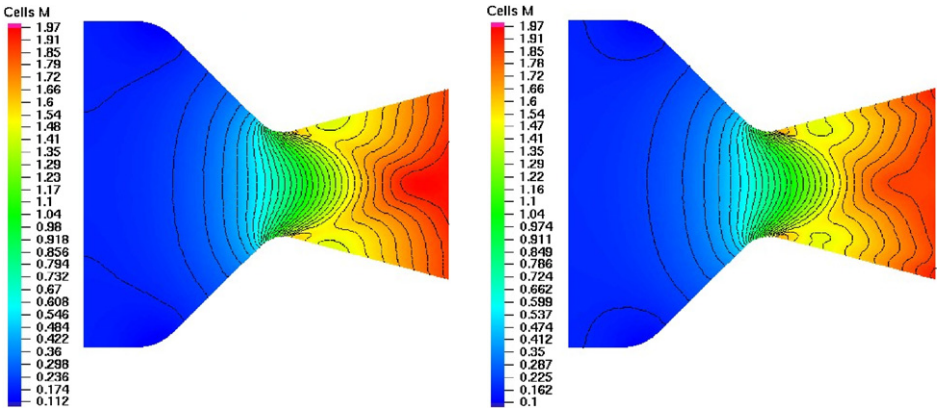

(a) $\phi = 0.1$, $d = 1\,\mu\text{m}$ (blue $= 0.1$, red $= 1.97$). (b) $\phi = 0.1$, $d = 20\,\mu\text{m}$. (blue $= 0.1$, red $= 1.93$).

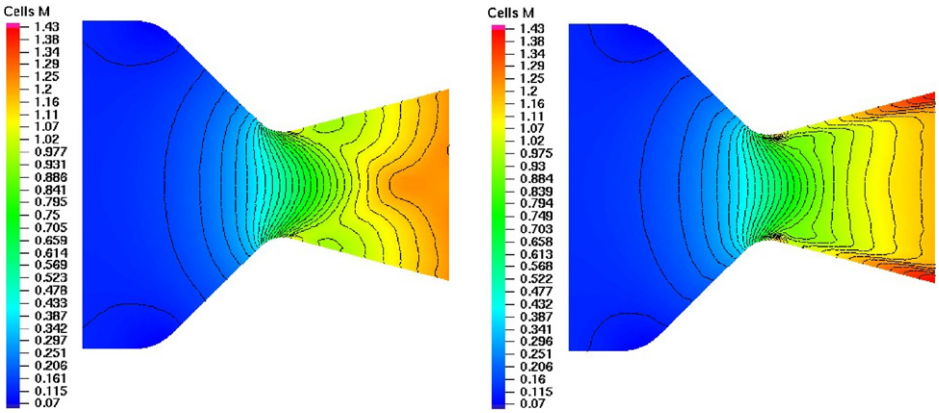

(c) $\phi = 0.5$, $d = 1\,\mu\text{m}$ (blue $= 0.07$, red $= 1.43$). (d) $\phi = 0.5$, $d = 20\,\mu\text{m}$ (blue $= 0.07$, red $= 1.43$).

Fig. 2. JPL nozzle: Mach numbers for $\phi = 0.1$, 0.5 and $d = 1\,\mu\text{m}$, $20\,\mu\text{m}$ (30 contours). (For interpretation of the references to colour in this figure legend, the reader is referred to the web version of this article.)

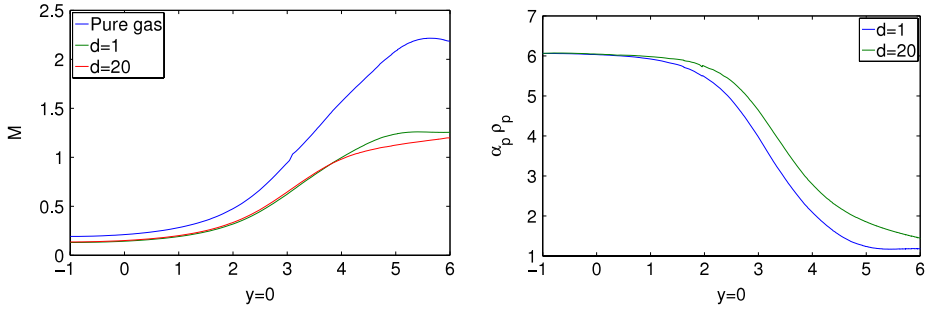

(a) Mach number. (b) Effective particle density.

Fig. 3. JPL nozzle: Effective particle density in $\frac{\text{kg}}{\text{m}^3}$ and Mach number at $\phi = 0.5$.

precisely due to the pressure gradient, and a larger amount of particles hit the wall. At the wall, the particles are deflected to the center of the nozzle by the boundary condition.

In contrast, the amount of particles in the vicinity of the walls in the diverging part of the nozzle decreases with increasing particle diameter, see Fig. 4. This can be explained from physical reasons in the same way as above. Moreover, the large particle Reynolds numbers at the throat (see Fig. 5(a)) cause less drag due to the drag curve in Fig. 5(b). Therefore, the larger particles are not able to follow the gas streamlines parallel to the walls. Nishida and Ishimaru [24], Chang [29], and Ishii and Umeda [26] claim that there are particle free layers in the vicinity of the walls, which increase with increasing particle size. In the present study, a small amount of particles is still present in the vicinity of the walls in the diverging part. Note that

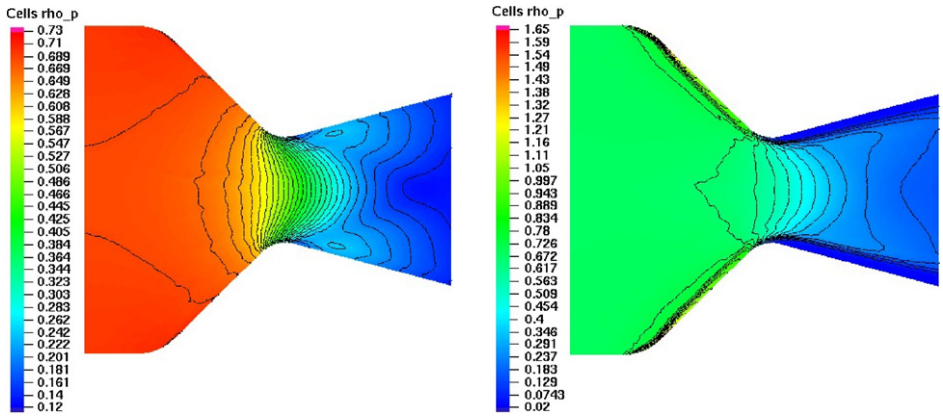

(a) $\phi = 0.1$, $d = 1\ \mu\text{m}$ (blue $= 0.13$, red $= 0.73$). (b) $\phi = 0.1$, $d = 20\ \mu\text{m}$ (blue $= 0.02$, red $= 1.65$).

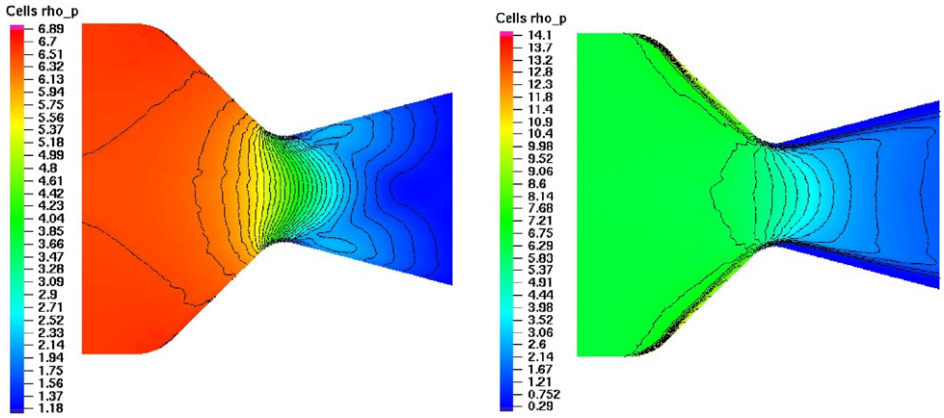

(c) $\phi = 0.5$, $d = 1\ \mu\text{m}$ (blue $= 1.18$, red $= 6.89$). (d) $\phi = 0.5$, $d = 20\ \mu\text{m}$ (blue $= 0.29$, red $= 14.1$).

Fig. 4. JPL nozzle: Effective particle densities in $\frac{\text{kg}}{\text{m}^3}$ for $\phi = 0.1, 0.5$ and $d = 1\ \mu\text{m}, 20\ \mu\text{m}$ (30 contours). (For interpretation of the references to colour in this figure legend, the reader is referred to the web version of this article.)

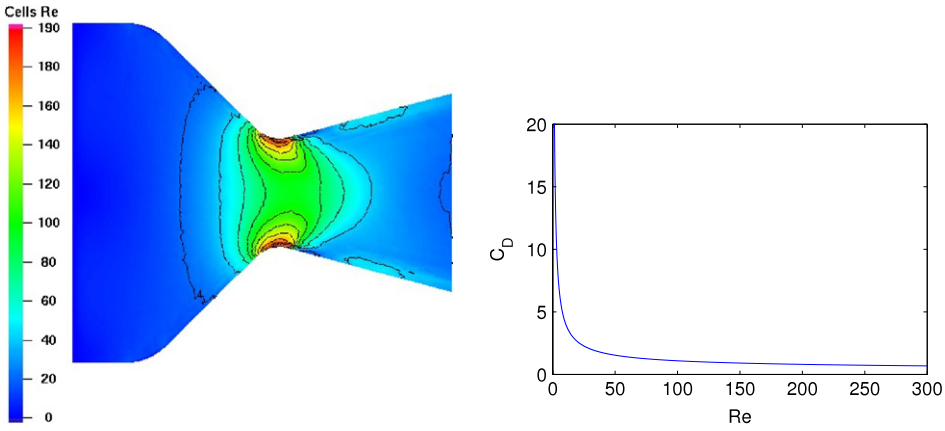

(a) Particle Reynolds number (blue $= 0$, red $= 190$). (b) Drag curve.

Fig. 5. Particle Reynolds number for $\phi = 0.5$, $d = 20\ \mu\text{m}$ (15 contours) and drag curve. (For interpretation of the references to colour in this figure legend, the reader is referred to the web version of this article.)

these particles vanish with decreasing mesh size, so that the added numerical diffusion can be seen as responsible for that phenomenon.

A comparison of Figs. 1(a), 2(c), and 4(c) with Figs. 2(d) and 4(d) illustrates the influence of the particle diameter. Since the smaller particles tend to mimic the gas behavior, the Mach number contour lines and those of the volume fraction are

Table 4
Free stream conditions of the oblique shock wave.

Quantity	Value	Unit
M_∞	2	
ρ_∞	6.0708	$\frac{\text{kg}}{\text{m}^3}$
P_∞	10^6	Pa
$\mathbf{v}_\infty$	$\sqrt{\frac{\gamma P_\infty}{\rho_\infty}}\begin{pmatrix} M_\infty \\ 0 \end{pmatrix}$	$\frac{\text{m}}{\text{s}}$
ϕ	0.1, 0.3	

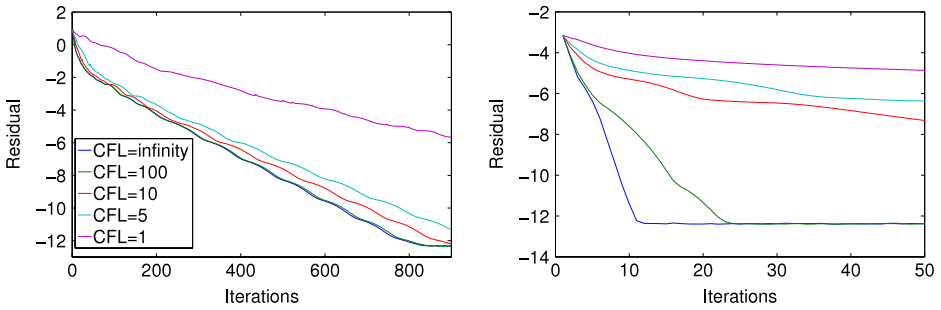

(a) High-resolution scheme. (b) Low-order scheme.

Fig. 6. JPL nozzle: Nonlinear convergence history in logarithmic scale for different CFL numbers on mesh level three.

essentially the same as the Mach number contours in a pure gas flow (compare Figs. 1(a), 2(c), and 4(c)). With increasing particle diameter the impact of drag decreases and the particles are less deflected to the outer boundaries of the diverging part of the nozzle. This affects the Mach number contours (compare Figs. 2(d) and 4(d)) since the volume fraction at the centerline is significantly higher than in the flow laden with smaller particles. To summarize the observations reported above, we state that the illustrated effects are physically sensible and compare well with the results reported in the literature.

Last but not least, we examine the convergence behavior of the nonlinear iteration for $\phi = 0.1$ and $d = 1\ \mu\text{m}$ to rate on the implicit scheme and particularly the boundary conditions. Note that in this case the interface momentum and heat exchange are rather large due to the small particle diameter. The convergence history of the low-order scheme presented in Fig. 6 is qualitatively comparable to the single-phase computations already discussed in [9,18]. Once again, the Newton-like scheme with CFL $= \infty$ exhibits the best convergence rates, while the convergence rates deteriorate with decreasing CFL numbers. For CFL $= \infty$ the residual falls below 10^{-12} in eleven iterations, while the residual hardly decreases for CFL $= 1$. This demonstrates the superior performance of the proposed boundary treatment and of the whole semi-implicit scheme in spite of the strong nonlinearity of the interfacial transfer terms. The excellent convergence behavior clearly justifies the use of implicit schemes.

In the computations with the high-resolution scheme convergence is also reached and unconditional stability can be observed. The results of the computations with CFL $= \infty$ and CFL $= 100$ are almost the same, while the former case exhibits slightly faster convergence. Obviously, the convergence rates deteriorate with decreasing CFL numbers. The convergence histories are qualitatively comparable with the single-phase computations [9,18]. Moderate CFL numbers also yield satisfactory convergence rates and the performance improvement with increasing CFL numbers stagnates at CFL $= 100$. Moreover, it is slightly less pronounced than in the single-phase gas computations. Two conflicting nonlinearities due to the interfacial exchange terms and the correction factors are present, which decelerates convergence. On the other hand, the deterioration of convergence rates due to the interfacial coupling remains relatively small. Nevertheless, the rate of convergence and the performance of the scheme are not affected for arbitrarily large CFL numbers, as observed in [13] even for the Euler equations.

6.2. Oblique shock reflection

The second test case in this chapter is a purely supersonic wave reflection at a ramp of angle 10°. In contrast to the JPL nozzle flow, a shock arises in the solution and is reflected at the ramp. At the supersonic inlet boundary (left side) the free stream conditions from Table 4 are prescribed, while no boundary condition is involved at the supersonic outlet boundary (right side). The upper and lower boundaries consist of solid walls. The goal of this section is to study the influence of the particle diameter as well as that of the mass fraction on the wave position. A comparison with a pure gas flow is performed for the purpose of code validation. Although the already analyzed JPL nozzle flow is a much more complicated test case, the current benchmark is also reported in the literature and allows an additional validation of the code in terms of the wave position. For a pure nitrogen flow, which is characterized by Table 1, the analytical solution downstream the shock can be

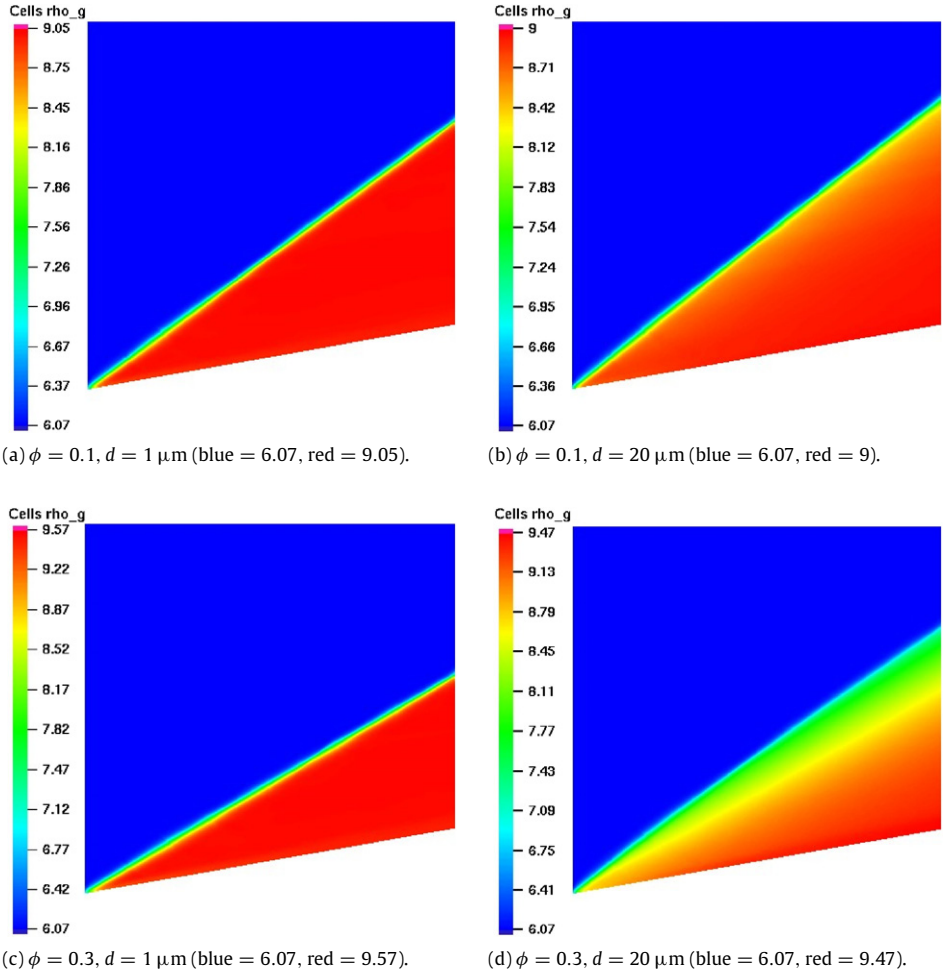

(a) $\phi = 0.1$, $d = 1\ \mu\text{m}$ (blue = 6.07, red = 9.05).

(b) $\phi = 0.1$, $d = 20\ \mu\text{m}$ (blue = 6.07, red = 9).

(c) $\phi = 0.3$, $d = 1\ \mu\text{m}$ (blue = 6.07, red = 9.57).

(d) $\phi = 0.3$, $d = 20\ \mu\text{m}$ (blue = 6.07, red = 9.47).

Fig. 7. Oblique shock: Effective gas density in $\frac{\text{kg}}{\text{m}^3}$ for $\phi = 0.1, 0.3$ and $d = 1\ \mu\text{m}, 20\ \mu\text{m}$. (For interpretation of the references to colour in this figure legend, the reader is referred to the web version of this article.)

determined by shock wave theory [47]. It reads

$$\rho_R = 8.8538\ \frac{\text{kg}}{\text{m}^3} \qquad M_R = 1.6405 \qquad P_R = 1706578.6040\ \text{Pa}$$

with wave angle $\beta = 39.3139^\circ$. The particulate phase consists of solid Al_2O_3 ceramic particles, which possess the physical properties listed in Table 1.

We compute numerical solutions of the configuration described so far for mass fractions $\phi = 0.1, 0.3$ and particle diameters $d = 1\ \mu\text{m}, 20\ \mu\text{m}$. Fig. 7 displays the effective gas densities, which are computed on an unstructured mesh consisting of 14,105 nodes and 27,904 triangles. The pure gas flow density is depicted in Fig. 8 (a) for comparison. We observe that the wave angle decreases with increasing mass fraction, while it increases with increasing particle diameter. The same observations on the wave position are reported in [48] and the decrease of the wave angle can be clearly observed by a comparison of Figs. 8(a), 7(a), (c) and (b), (d). At the same time the increase of the wave angle due to increasing particle diameter is less obvious in Fig. 7 but still present and also observed in [48]. An increasing particle diameter has an additional effect on the gas phase. Fig. 7 illustrates a smearing of the shock in the gas phase for larger particles. At first glance this seems to be due to an additional amount of diffusion. This behavior can in fact be explained by the physical nature of the particles. The particulate phase, if it is considered isolated, does not exhibit a shock at that position due to the lack of pressure. Moreover, it was already pointed out in Section 6.1 that large particles are less inclined to follow the gas streamlines. The particle Reynolds number distribution (see Fig. 8(b)) exhibits large values in the vicinity of the shock, which results in less drag (compare Fig. 5(b)) and clearly justifies the above explanation. At the same time, interfacial drag is still present and its magnitude and influence on the gas phase increases with increasing particle mass fraction. Hence, the shock in the gas phase is smeared and smoothed out by the influence of the particulate phase rather than by additional numerical diffusion.

Finally, we examine the convergence of the nonlinear iteration by a comparison of different CFL numbers for computations on a mesh consisting of 3565 nodes and 6976 triangles. The developed scheme turns out to be unconditionally

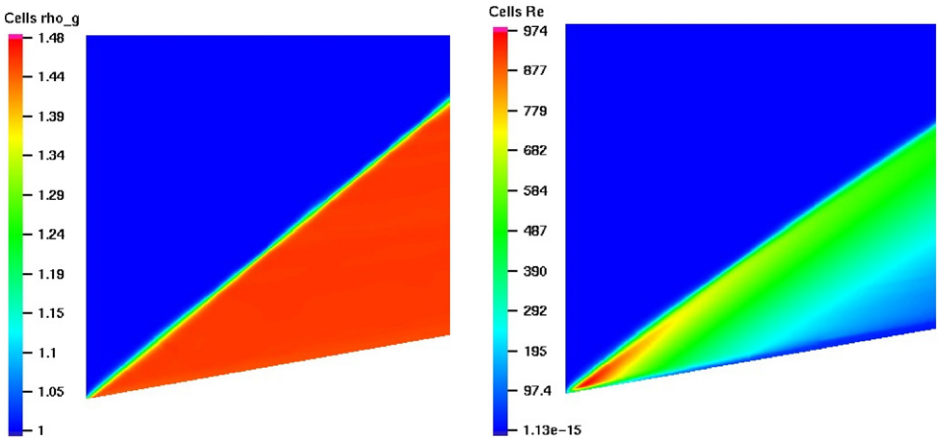

(a) Pure gas (blue = 6.07, red = 9.05). (b) Particle Reynolds number (blue = 0, red = 974).

Fig. 8. Oblique shock: Pure gas flow density in $\frac{\text{kg}}{\text{m}^3}$ and particle Reynolds number with $\phi = 0.3$, $d = 20\ \mu\text{m}$. (For interpretation of the references to colour in this figure legend, the reader is referred to the web version of this article.)

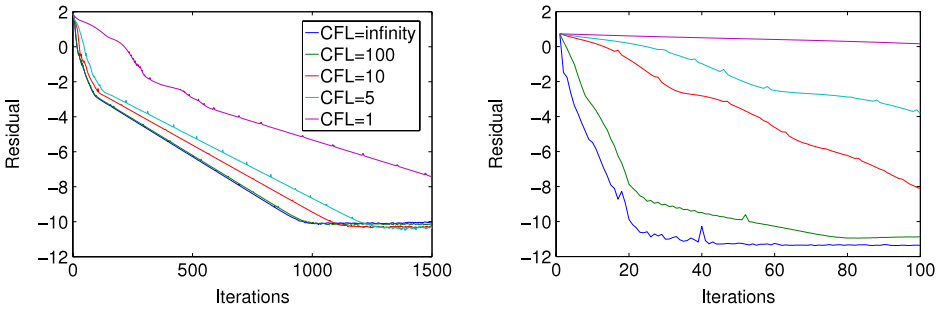

(a) High-resolution scheme. (b) Low-order scheme.

Fig. 9. Oblique shock: Nonlinear convergence histories in logarithmic scale.

stable for a suitable initial guess, which is provided by the low-order solution. To initialize the low-order computations a few pre-iterations with CFL = 10 are performed. Fig. 9 shows the convergence histories for both schemes and the convergence behavior is qualitatively comparable to the formerly reported test cases. In the case of the low-order scheme the rate of convergence improves with increasing CFL number, while CFL = ∞ produces the best results since the relative error falls to 10^{-11} in about 40 iterations. In a simulation with CFL = 1, it hardly decreases in the first 100 iterations. The high-resolution scheme exhibits a similar behavior. Also in this case, the choice of CFL = ∞ offers the fastest convergence. The relative error falls to 10^{-8} in about 600 iterations after which the solution can be considered stationary, while CFL = 100 results in nearly the same rate of convergence. However, the rate of convergence deteriorates with decreasing CFL numbers.

In summary, the choice of large CFL numbers is usually preferable since the scheme proves to be unconditionally stable in practical computations for a suitable initial condition, which can be easily obtained in terms of the low-order solution. No parameter in the developed scheme is required and it inherits the convergence behavior of the single-phase gas code in a qualitative sense.

6.3. Operator splitting vs. fully coupled solution strategy

There are two basic approaches to an implicit numerical treatment of the interfacial transfer terms. Either operator splitting techniques as presented in Section 5.1 and applied in [38] to stationary as well as non-stationary problems may be employed, or the equations may be integrated in time by the fully coupled implicit time integration as discussed in Chapter 5.2. At first glance, the former approach significantly reduces the computational costs since the arising algebraic systems can be solved separately. In comparison with the fully coupled approach, where an 8 NVT × 8 NVT-system must be solved, operator splitting reduces the computational effort to the solution of two algebraic systems of size 4 NVT × 4 NVT and a source term integration step. Operator splitting of Yanenko type is rather stable and robust but not suitable for the computation of stationary solutions. It does not allow the solution to approach steady state and the final result depends on the (pseudo) time step. Douglas–Rachford operator splitting (see Section 5.1.2) is therefore investigated, while the Yanenko splitting may serve to compute an initial guess. The Douglas–Rachford splitting is known to be very robust at least in the framework of alternating direction implicit (ADI) iterative solvers.

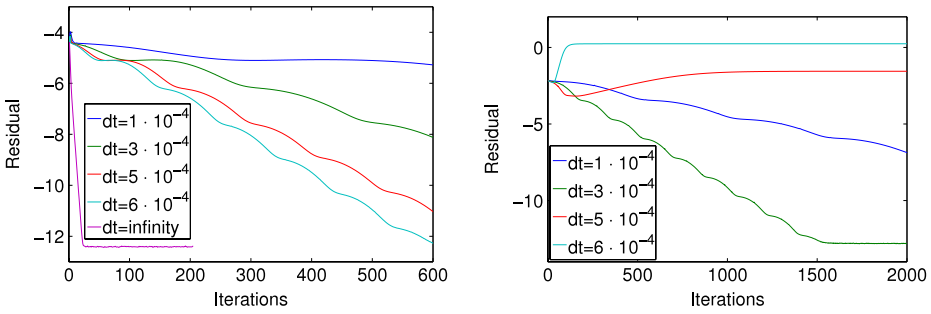

(a) Fully coupled scheme. (b) Douglas–Rachford splitting.

Fig. 10. Nonlinear convergence history in logarithmic scale of the low-order schemes for different pseudo time steps on mesh level three.

It follows from the numerical results that the Douglas–Rachford splitting introduces an upper bound for the pseudo time step, which hampers the convergence to steady state. This turns the promising reduction of computational costs into a drawback due to the increasing number of nonlinear iterations arising by restrictive time step constraints. Note that in a time-dependent application, where rather small time steps are essential for accuracy reasons, operator splitting is still competitive due to the low costs.

For the comparison of the fully coupled and the operator splitting approach both schemes were applied to the problem reported in Section 6.1 on mesh level three. Mass fractions of $\phi = 0.5$ and particle diameters of $d = 20\ \mu\text{m}$ are prescribed for the numerical tests. The logarithmic plots of nonlinear convergence histories produced by both the fully coupled and the operator splitting approach are presented in Fig. 10. All computations are based on the low-order scheme, which is sufficient to examine the treatment of source terms. Obviously, the convergence of the fully coupled approach is far superior since it enables the use of large CFL numbers. On the contrary, the Douglas–Rachford splitting exhibits convergence only for small pseudo time steps. The scheme remains stable and does not converge for moderate CFL numbers, which can be explained by the large stiffness of the interfacial forces and the explicit treatment in the hyperbolic step. Since it is a well known fact that decoupled methods are subject to time step restrictions, the observations are as expected. The fully coupled implicit scheme converges in about 15 iterations for $\text{CFL} = \infty$ and exhibits convergence for all applied pseudo time steps. In contrast, Douglas–Rachford splitting does not converge for $\Delta t > 3 \cdot 10^{-4}$, which corresponds to a maximal CFL number of about $\text{CFL} = 9$. However, it converges for $\Delta t = 3 \cdot 10^{-4}$ in approximately 1500 iterations. This corresponds to 75 times more iterations compared to the fully coupled scheme.

7. Conclusions and outlook

A high-resolution finite element scheme was proposed for the macroscopic two-fluid model of particle-laden gas flows. The main highlight is a robust iterative solver that delivers converged steady-state solutions despite oscillatory correction factors even if stiff algebraic source terms are present. The semi-implicit pseudo time stepping appears to be unconditionally stable and reduces to a Newton-like method in the limit of infinite CFL numbers. With increasing time steps the convergence rates improve and they do not deteriorate if the CFL number exceeds some upper bound. The fully coupled solver was compared to operator splitting techniques and was shown to be much more robust than the latter approaches. The Galerkin finite element discretization was equipped with weak boundary conditions of Neumann type based on a boundary Riemann solver for the inlets and outlets and a penalty term was added to prevent the flow from penetrating solid walls. Summarizing the results of the presented numerical study, we conclude that the unconditional stability of the fully coupled implicit time integration proposed in this paper makes it a highly promising solution strategy for the two-fluid model.

The convergence to steady state can be further accelerated within the framework of a nonlinear (FAS-FMG) multigrid method. Further tasks to be accomplished include the implementation of the new algorithm in three dimensions, its combination with adaptive mesh refinement techniques, and application to real-life problems. Moreover, the computational model will be extended to viscous flows.

Acknowledgment

The authors gratefully acknowledge the financial support by the German Research Foundation (DFG) within the framework of the Collaborative Research Center SFB 708.

References

[1] D. Kuzmin, On the design of general purpose flux limiters for finite element schemes. I. Scalar convection, J. Comput. Phys. 219 (2006) 513–531.
[2] D. Kuzmin, Algebraic flux correction for finite element discretizations of coupled systems, in: E. Onate, M. Papadrakakis, B. Schrefler (Eds.), Comp. Meth. for Coupled Prob. in Sc. and Eng. II, CIMNE, 2007, pp. 653–656.

[3] D. Kuzmin, M. Möller, Algebraic flux correction I. Scalar conservation laws, in: D. Kuzmin, R. Löhner, S. Turek (Eds.), Flux-Corrected Transport, Principles, Algorithms, and Applications, Springer, 2005, pp. 155–206.
[4] D. Kuzmin, M. Möller, Algebraic flux correction II. Compressible Euler equations, in: D. Kuzmin, R. Löhner, S. Turek (Eds.), Flux-Corrected Transport, Principles, Algorithms, and Applications, Springer, 2005, pp. 207–250.
[5] D. Kuzmin, Explicit and implicit FEM-FCT algorithms with flux linearization, J. Comput. Phys. 228 (2009) 2517–2534.
[6] D. Kuzmin, S. Turek, High-resolution FEM-TVD schemes based on a fully multidimensional flux limiter, J. Comput. Phys. 198 (1) (2004) 131–158.
[7] D. Kuzmin, M. Möller, J. Shadid, M. Shashkov, Failsafe flux limiting and constrained data projections for systems of conservation laws, J. Comput. Phys. 229 (2010) 8780–8801.
[8] V. John, E. Schmeyer, Finite element methods for time-dependent convection–diffusion–reaction equations with small diffusion, Comput. Methods Appl. Mech. Engrg. 198 (2008) 475–494.
[9] M. Gurris, Implicit finite element schemes for compressible gas and particle-laden gas flows, Ph.D. Thesis, Dortmund, 2009.
[10] V. Dolejší, M. Feistauer, A semi-implicit discontinuous Galerkin finite element method for the numerical solution of inviscid compressible flow, J. Comput. Phys. 198 (2004) 727–746.
[11] M. Feistauer, V. Kučera, On a robust discontinuous Galerkin technique for the solution of compressible flow, J. Comput. Phys. 224 (2007) 208–231.
[12] A. Nejat, A higher-order accurate unstructured finite volume Newton-Krylov algorithm for inviscid compressible flows, Ph.D. Thesis, Vancouver, 2007.
[13] J.-Y. Trépanier, M. Reggio, D. Ait-Ali-Yahia, An implicit flux-difference splitting method for solving the Euler equations on adaptive triangular grids, Internat. J. Numer. Methods Heat Fluid Flow 3 (1993) 63–77.
[14] L. Sainsaulieu, Finite volume approximation fo two phase-fluid flows based on an approximate Roe-type Riemann solver, J. Comput. Phys. 121 (1995) 1–28.
[15] T. Saito, Numerical analysis of dusty-gas flows, J. Comput. Phys. 176 (2002) 129–144.
[16] M. Pelanti, R.J. LeVeque, High-resolution finite volume methods for dusty gas jets and plumes, SIAM J. Sci. Comput. 28 (4) (2006) 1335–1360.
[17] R. Saurel, R. Abgrall, A multiphase Godunov method for compressible multifluid and multiphase flows, J. Comput. Phys. 150 (1999) 425–467.
[18] M. Gurris, D. Kuzmin, S. Turek, Implicit finite element schemes for the stationary compressible Euler equations, Internat. J. Numer. Methods Fluids (2010) in press (doi:10.1002/fld.2532).
[19] D.A. Drew, S.L. Passmann, Theory of Multicomponent Fluids, Springer, 1999.
[20] M. Ishii, T. Hibiki, Thermo-Fluid Dynamics of Two-Phase Flow, Springer, 2006.
[21] H. Städke, Gasdynamic Aspects of Two-Phase Flow, Wiley, 2006.
[22] D. Kuzmin, Numerical simulation of reactive bubbly flows, Ph.D. Thesis, University of Jyväskylä, 1999.
[23] A. Sokolichin, Mathematische Modellbildung und Numerische Simulation von Gas–Flüssigkeits–Blasenströmungen, German, Habilitation Thesis, Stuttgart, 2002.
[24] M. Nishida, S. Ishimaru, Numerical analysis of gas–solid two-phase nonequilibrium nozzle flows, JSME Int. J. II 33 (3) (1990) 494–500.
[25] S. Sivier, E. Loth, R. Baum, R. Löhner, Unstructured adaptive remeshing finite element method for dusty shock flow, Shock Waves (3) (1999) 15–23.
[26] R. Ishii, Y. Umeda, Nozzle flows of gas-particle mixtures, Phys. Fluids 30 (3) (1987) 752–760.
[27] J.S. Park, S.W. Beak, Interaction of a moving shock wave with a two-phase reacting medium, Int. J. Heat Mass Transfer 46 (2003) 4117–4732.
[28] S.-W. Kim, K.-S. Chang, Reflection of shock wave from a compression corner in a particle-laden gas, Shock Waves 1 (1991) 65–73.
[29] I. Chang, One- and two-phase nozzle flows, AIAA J. 18 (12) (1980) 1445–1461. Article No. 80-0272R.
[30] O. Igra, G. Hu, J. Falcovitz, B.Y. Wang, Shock wave reflection from a wedge in a dusty gas, Int. J. Multiphase Flow 30 (2004) 1139–1169.
[31] O. Borchers, C. Busch, A. Sokolichin, G. Eigenberger, Applicability of the standard k–ϵ turbulence model to the dynamic simulation of bubble columns. Part II: comparison of detailed experiments and flow simulations, Chem. Eng. Sci. 54 (1999) 5927–5935.
[32] M. Sommerfeld, The unsteadyness of shock waves propagating through gas-particle mixtures, Exp. Fluids 3 (4) (1985) 197–206.
[33] J.G. Knudsen, D.L. Katz, Fluid Mechanics and Heat Transfer, McGraw-Hill, New York, 1958.
[34] E. Godlewski, P.A. Raviart, Numerical Approximation of Hyperbolic Systems of Conservation Laws, Springer Verlag, 1995.
[35] C.A.J. Fletcher, The group finite element formulation, Comput. Methods Appl. Mech. Engrg. 37 (1983) 225–243.
[36] A. Bermúdez, M.E. Vázquez, Upwind methods for hyperbolic conservation laws with source terms, Comput. & Fluids 23 (8) (1994) 1049–1071.
[37] J.W. Banks, W.D. Henshaw, J.N. Shadid, An evaluation of the FCT method for high-speed flows on structured overlapping grids, J. Comput. Phys. 228 (15) (2009) 5349–5369.
[38] M. Gurris, D. Kuzmin, S. Turek, Finite element simulation of particle-laden gas flows, J. Comput. Appl. Math. 233 (12) (2010) 3121–3129.
[39] V. John, A. Liakos, Time-dependent flow across a step: the slip with friction boundary condition, Internat. J. Numer. Methods Fluids 50 (2006) 713–731.
[40] L. Demkowicz, J.T. Oden, W. Rachowicz, O. Hardy, An $h-p$ Taylor–Galerkin finite element method for compressible Euler equations, Comput. Methods Appl. Mech. Engrg. 88 (1991) 363–396.
[41] M. Utku, G.F. Carey, Boundary penalty techniques, Comput. Methods Appl. Mech. Engrg. 30 (1982) 103–118.
[42] F. Schieweck, On the role of boundary conditions for CIP stabilization of higher order finite elements, Preprint, 2007.
[43] Y. Bazilevs, T.J.R. Hughes, Weak imposition of Dirichlet boundary conditions in fluid mechanics, Comput. & Fluids 36 (2007) 12–26.
[44] P.R.M. Lyra, Unstructured grid adaptive algorithms for fluid dynamics, Ph.D. Thesis, Swansea, 1994.
[45] R.J. LeVeque, Numerical Methods for Conservation Laws, in: Lectures in mathematics, Birkhäuser, 1992.
[46] J. Douglas, H.H. Rachford, On the numerical solution of heat conduction problems in two or three space variables, Trans. Amer. Math. Soc. 82 (1956) 421–439.
[47] J.D. Anderson, J.C. Tannenhill, R.H. Plecher, Modern Compressible Flow with Historical Perspective, in: Series Aeronautical and Aerospace Engineering, McGraw-Hill Publishing Company, 1990.
[48] G.A. Saltanov, Neravnovesniye I Nestacionarniye Processy V Gazodinamike Odnofaznih I Dvuhfaznih Sred, Springer, Moscow, 1979 (in Russian).